Geosci. Model Dev. Discuss., doi:10.5194/gmd-2016-181, 2016
Manuscript under review for journal Geosci. Model Dev.
Published: 19 August 2016
© Author(s) 2016. CC-BY 3.0 License.

Geoscientific Model Development Discussions
Open Access

Development of CarbonTracker Europe-CH_4 – Part 1: system set-up and sensitivity analyses

Aki Tsuruta[1], Tuula Aalto[1], Leif Backman[1], Janne Hakkarainen[2], Ingrid T. van der Laan-Luijkx[3], Maarten C. Krol[3,5,6], Renato Spahni[4], Sander Houweling[5,6], Marko Laine[2], Marcel van der Schoot[7], Ray Langenfelds[7], Raymond Ellul[8], Wouter Peters[3,9]

[1]Climate Research, Finnish Meteorological Institute, Helsinki, Finland
[2]Earth Observation, Finnish Meteorological Institute, Helsinki, Finland
[3]Meteorology and Air Quality, Wageningen University, Wageningen, the Netherlands
[4]Climate and Environmental Physics, Physics Institute, and Oeschger Centre for Climate Change Research, University of Bern, Bern, Switzerland
[5]SRON Netherlands Institute for Space Research, Utrecht, the Netherlands
[6]Institute for Marine and Atmospheric Research, Utrecht University, Utrecht, the Netherlands
[7]CSIRO Oceans and Atmosphere, Aspendale, Australia
[8]Atmospheric Research, Department of Geosciences, University of Malta, Msida, Malta
[9]Centre for Isotope Research, University of Groningen, Groningen, the Netherlands

Correspondence to: Aki Tsuruta (Aki.Tsuruta@fmi.fi)

Abstract. CarbonTracker Europe-CH_4 (CTE-CH_4) inverse model versions 1.0 and 1.1 are presented. The model optimizes global surface methane emissions from biosphere and anthropogenic sources using an ensemble Kalman filter (EnKF) based optimization method, using the TM5 chemistry transport model as an observation operator, and assimilating global in-situ atmospheric methane mole fraction observations. In this study, we examine sensitivity of our CH_4 emission estimates on the ensemble size, covariance matrix, prior estimates, observations to be assimilated, assimilation window length, convection scheme in TM5, and model structure in the emission estimates by performing CTE-CH_4 with several set-ups. The analyses show that the model is sensitive to most of the parameters and inputs that were examined. Firstly, using a large enough ensemble size stabilises the results. Secondly, using an informative covariance matrix reduces uncertainty estimates. Thirdly, agreement with discrete observations became better when assimilating continuous observations. Finally, the posterior emissions were found sensitive to the choice of prior estimates, convection scheme and model structure, particularly to their spatial distribution. The distribution of posterior mole fractions derived from posterior emissions is consistent with the observations to the extent prescribed in the various covariance estimates, indicating a satisfactory performance of our system.

1 Introduction

Inverse modelling is a popular tool to estimate global to regional scale surface greenhouse gas fluxes. The models are often based on assimilation techniques, where surface emissions are constrained by measurements of atmospheric mole fractions.

Geosci. Model Dev. Discuss., doi:10.5194/gmd-2016-181, 2016
Manuscript under review for journal Geosci. Model Dev.
Published: 19 August 2016
© Author(s) 2016. CC-BY 3.0 License.

The inversion method can provide information on the emissions, consistent with measurements of atmospheric mole fractions. This allows greenhouse gas emissions to be studied in areas where local measurements are absent, and environmental drivers of emissions are unknown. Furthermore, greenhouse gas emission estimates are uncertain because not all processes related to gas emissions and uptakes are understood. Using inversion methods, we are generally able to reduce uncertainties in existing estimates.

Several inverse models have recently been developed to estimate global methane (CH_4) surface emissions (e.g. Bergamaschi *et al.* (2009), LMDZ-MIOP (Bousquet *et al.*, 2006) LMDZt-SACS (Pison *et al.*, 2009; Bousquet *et al.*, 2011), CarbonTracker-CH_4 (Bruhwiler *et al.*, 2014; Tsuruta *et al.*, 2015), GEOS-Chem (Fraser *et al.*, 2013), MATCH model (Chen and Prinn, 2006)). Those models differ in many ways, such as optimization technique (e.g. an adjoint model 4DVAR, ensemble Kalman smoother/filter), transport model (e.g. TM5, LMDZ, GEOS-Chem, MATCH) that is used as an observation operator, prior emission estimates, and set of observations assimilated to constrain the emissions. Although the inverse modelling technique has the advantage that the estimates are consistent with the observations, the emission estimates can vary between the models (Kirschke *et al.*, 2013). Therefore, independent estimates would be useful to further understand the trends and spatial patterns of methane emissions and its atmospheric concentrations, and relations between the two. Furthermore, the estimates can vary not only between the models, but also depending on the model settings.

Ideally, different inverse models should be able to produce the same emission estimates regardless of prior estimates. Bergamaschi *et al.* (2010, 2013) showed sensitivity of the derived emission estimates, but found that it was not significant for regional and global estimates. However, at regional scale, spatial distribution is dependent on the prior estimates. Therefore, it is important to include as much information as possible about the spatial distributions in the prior emission estimates for those models that optimizes emissions region-wise (Bruhwiler *et al.*, 2014; Tsuruta *et al.*, 2015). Because of the nature of inverse models that are constrained by the observations, it is very important to use observations that cover the domain of interest in time and space well. Previous studies showed that increasing the number of methane observations improved the emission estimates (Beck *et al.*, 2012; Bergamaschi *et al.*, 2013; Houweling *et al.*, 2014; Fraser *et al.*, 2013). Furthermore, Locatelli *et al.* (2013) addressed the impacts of the transport model by comparing flux estimates made with the same system, but with different transport models. Although the estimates agreed well for the global total, regional estimates differed by 23-48%. All of these impacts may vary between the models, and the total differences are more than the sum of each part, and an impact in a certain set-up may not be quantified by estimating it in another set-up. Therefore, it is important to assess those impacts when setting up a new model, such as our attempt here.

In this study, we present impact of parameters and inputs on methane emission estimates using the CarbonTracker Europe-CH_4 (CTE-CH_4) model. CTE-CH_4 is a methane version of CarbonTracker (Peters *et al.* 2005), originally developed to optimize global CO_2 fluxes by NOAA-ESRL (National Oceanic and Atmospheric Administration's Earth System Research

Geosci. Model Dev. Discuss., doi:10.5194/gmd-2016-181, 2016
Manuscript under review for journal Geosci. Model Dev.
Published: 19 August 2016
© Author(s) 2016. CC-BY 3.0 License.

Laboratory) and Wageningen University, the Netherlands. CarbonTracker was later implemented for CH_4 by the NOAA-ESRL (Bruhwiler *et al.*, 2014) and the Finnish Meteorological Institute (FMI) (Tsuruta *et al.*, 2015). CTE-CH_4 is based on an ensemble Kalman filter (EnKF; Evensen, 2003) optimization technique and uses the TM5 atmospheric chemistry transport model as an observation operator. EnKF is a widely applied method in inverse models, when the dimension of the state vector and hence its covariance matrix is large. TM5 is a well-established atmospheric transport model that is used both as a forward model and an observation operator in many other systems, and is under active development. CTE-CH_4 optimises anthropogenic and biosphere methane emission estimates, constrained by global in-situ atmospheric CH_4 mole fraction observations. CTE-CH_4 is built to work well globally, but has its focus on Europe. The zoom of TM5 is applied over Europe, where the observation network is dense. Furthermore, Europe is divided into four sub-regions in which the fluxes are optimised separately.

As CTE-CH_4 is an EnKF based system, we assessed the impacts of ensemble size and state vector covariance matrix using several ensemble sizes and two different covariance matrices. Furthermore, in order to assess the impacts of prior emission estimates, observations, transport model, and the model structure, we performed CTE-CH_4 using two sets of biosphere prior emission estimates, two sets of observations, two convection schemes in TM5, and two versions of the CTE-CH_4 model. To limit the computational cost, summer 2007 was selected as a study period. The aim of this study is to introduce the set-up and choices made for an optimally working methane inversion system, which will later be used in long term studies of global and regional methane emissions and their trends presented in an accompanying paper (Tsuruta *et al.*, 2016). The results and evaluation of longer time series (recent decade), comparison between two model structures, and detailed analysis on estimates over Europe will be discussed in the second part of this paper.

2. Methods and datasets

2.1 CTE-CH_4 data assimilation system

CTE-CH_4 is a data assimilation system that optimizes global surface methane emissions by minimizing a cost function:

$$J = (\boldsymbol{x} - \boldsymbol{x^b})^T \boldsymbol{P}^{-1} (\boldsymbol{x} - \boldsymbol{x^b}) + (\boldsymbol{y} - H(\boldsymbol{x}))^T \boldsymbol{R}^{-1} (\boldsymbol{y} - H(\boldsymbol{x})) \quad (1)$$

$$\boldsymbol{E} = G(\boldsymbol{x}) \boldsymbol{E^b} \quad (2)$$

where $\boldsymbol{x}$ (dimension N) is a state vector that contains a set of scaling factors that multiply the CH_4 surface emissions ($\boldsymbol{E}$, dimension 360×180) that we want to improve starting from a prior estimate of these emissions ($\boldsymbol{E^b}$ [360×180]) and scaling factors $\boldsymbol{x^b}$ [N]. $\boldsymbol{P}$ [N×N] is the covariance matrix of the state vector, $\boldsymbol{y}$ (dimension M) is a vector of atmospheric methane mole fraction observations, $\boldsymbol{R}$ [M×M] is a covariance matrix of the observations $\boldsymbol{y}$, and H is an observation operator [M×N]. The operator G transforms the regionally estimated scaling factors $\boldsymbol{x}$ to a 1°×1° global map, which are used to scale prior emissions $\boldsymbol{E}$. The cost function in Eq. (1) is minimized using an ensemble Kalman filter (EnKF) (Evensen, 2003) with 500

Geosci. Model Dev. Discuss., doi:10.5194/gmd-2016-181, 2016
Manuscript under review for journal Geosci. Model Dev.
Published: 19 August 2016
© Author(s) 2016. CC-BY 3.0 License.

ensemble members, and the TM5 chemistry transport model (Krol *et al.*, 2005) was used as an observation operator that transforms emissions $\boldsymbol{E}$ into simulated CH_4 mole fractions ($H(\boldsymbol{x})$). The emissions $\boldsymbol{E}$ were optimized weekly, with an assimilation window length of 5 weeks.

The optimal weekly mean CH_4 fluxes F_{tot} at region r, and time (week) t were calculated as follows:

$$F_{tot}(r,t) = \lambda_{bio}(r,t) \times F_{bio}(r,t) + \lambda_{anth}(r,t) \times F_{anth}(r,t) + F_{fire}(r,t) + F_{term}(r,t) + F_{oce}(r,t) \qquad (1)$$

where F_{bio}, F_{ant}, F_{fire}, F_{term}, F_{oce}, are the prior emissions from biosphere, anthropogenic activities, fire, termites and ocean, respectively.

The regional definition of CTE-CH_4 is defined based on modified TransCom (mTC) and land-ecosystem regions (Fig. 1). The mTC regions were defined similarly to Tsuruta *et al.* (2015). Land-ecosystem regions in 1°×1° grid were defined based on Prigent *et al.* (2007) and Wania *et al.* (2010), as in the LPJ-WHyME vegetation model (Spahni *et al.* 2011), and contains six land ecosystem types (LET): inundated wetland and peatland (IWP), wet mineral soil (WMS), rice (RIC), anthropogenic land (ANT), water (WTR) and ice (ICE). WTR is defined similarly to Peters *et al.* (2007), and the ICE region corresponds to the ice region in the mTC definition. The rest of land-ecosystem regions were defined according to the fraction of IWP, WMS and RIC used in LPJ-WHyME. To limit the number of degrees of freedom, only one dominant LET was assigned to each grid cell. In the following cases, LET with the largest fraction was chosen. For grid cells where fraction of IWP, WMS or RIC is larger than 0.1, either IWP, WMS or RIC was assigned. For grid cells where the fraction of IWP or WMS are smaller than 0.1, and the prior anthropogenic emission estimates (EDGARv4.2 FT2010, see Section 2.3) including emissions from rice fields are zero, IWP or WMS was assigned. Furthermore, if the LPJ-WHyME biosphere emission estimates are much larger than the EDGARv4.2 FT2010 emission estimates (more than 200%), either IWP or WMS was assigned. On the other hand, if the EDGARv4.2 FT2010 emission estimates were much larger than LPJ-WHyME biosphere emission estimates, either ANT, RIC or WTR were assigned.

For the baseline model (M1), biosphere emissions were optimized in regions where LET are either IWP or WMS (i.e. $\lambda_{anth}(r,t) = 0$), and anthropogenic emissions were optimized in regions where LET are RIC, ANT or WTR (i.e. $\lambda_{bio}(r,t) = 0$). This approach resulted in 28 biosphere regions and 30 anthropogenic regions, i.e. 58 scaling factors $\boldsymbol{\lambda}(\boldsymbol{t}) = (\boldsymbol{\lambda}_{bio}(\boldsymbol{t}), \boldsymbol{\lambda}_{anth}(\boldsymbol{t}))$ to be optimized per week globally. This number of scaling factors is smaller than theoretically expected (16 mTC regions × 5 land-ecosystem regions = 80 scaling factors) because some mTC regions contain less than five ecosystems types. For comparison, we developed a model where both $\lambda_{bio}(r,t)$ and $\lambda_{anth}(r,t)$ are optimized in each region (M2). In M2, the regional definition of the scaling factors for the biosphere emissions is based on the combination of mTC and land-ecosystem regions (58 regions), and for the anthropogenic emissions, the mTC region (15 regions) is used. This results in 74 scaling factors to be optimized per week globally in M2. Note that scaling factors are estimated purely

Geosci. Model Dev. Discuss., doi:10.5194/gmd-2016-181, 2016
Manuscript under review for journal Geosci. Model Dev.
Published: 19 August 2016
© Author(s) 2016. CC-BY 3.0 License.

mathematically in EnFK, and there is no system to choose which scaling factors ($\lambda_{bio}(r,t)$ or $\lambda_{anth}(r,t)$) gain larger weights based on physical or meteorological properties.

2.2 TM5 atmospheric chemistry transport model

The link between atmospheric CH_4 observations and the exchange of CH_4 at Earth's surface is transport in the atmosphere. In our data assimilation system, the TM5 chemistry transport model version 3.0 (Krol *et al.*, 2005; Huijnen *et al.*, 2010) was applied as the observation operator. TM5 was run with a 1°×1° (latitude x longitude) zoom region over Europe (24°N to 74°N, 21°W to 45°E), framed by an intermediate zoom region of 2°×3°, and a global 4°×6° degree resolution, driven by 3-hourly ECMWF ERA-Interim meteorological fields with 25 vertical layers. The main sink of CH_4, atmospheric chemical methane loss by OH in the troposphere, was calculated using off-line chemistry with monthly tropospheric OH concentrations concentrations based on Spivakovsky (2000) scaled by 0.92 (Houweling *et al.*, 2014), based on the inversion study by Huijnen *et al.* (2010). Furthermore, stratospheric methane sinks due to reaction with OH, Cl and $O(^1D)$ were included by applying reaction rates based on the 2D photochemical Max-Planck-Institute (MPI) model (Brühl and Crutzen, 1993). The global total atmospheric chemical loss, i.e. the integrated OH, Cl and $O(^1D)$ losses during the test period was 229 Tg CH_4 (per 154 days).

In order to avoid influence of initial condition of atmospheric concentrations, TM5 was run as a forward mode for model year of 2007, starting from uniform mole fraction of 1600 ppb globally and using prior emission estimates. Using its final values, i.e. assigning the values of the end of the model year as an initial condition, TM5 was run once again in a forward mode for 2007. Using the second final values, CTE-CH_4 was run starting from the beginning of 2007 up to June 2007 using set-up S1 (see Section 3.2) to get well-mixed initial atmospheric concentrations for the experiments presented in this study.

TM5 was recently equipped with two versions of convection schemes. A version based on Tiedtke (1989), and another version that takes the convection mass fluxes directly from ECMWF ERA-Interim (Gregory *et al.*, 2000). The latter approach has a stronger convection in the northern hemisphere during summer, producing lower concentrations near the surface, and higher concentrations in the free troposphere and lower stratosphere compared to the former version (Olivie *et al.*, 2004).

2.3 Prior CH_4 flux datasets

The prior methane emission estimates F_{anth}, F_{bio}, F_{fire} and F_{term} in Eq. (1) were collected from inventories and previous studies. All emission fields were processed to match the finest TM5 resolution, i.e. 1°×1° (latitude × longitude), globally. The total prior emissions for each category are given in Table 3.

Geosci. Model Dev. Discuss., doi:10.5194/gmd-2016-181, 2016
Manuscript under review for journal Geosci. Model Dev.
Published: 19 August 2016
© Author(s) 2016. CC-BY 3.0 License.

Anthropogenic methane emissions are responsible for more than half of the global methane source. For monthly mean anthropogenic emissions, the Emission Database for Global Atmospheric Research version 4.2 (EDGARv4.2) FT2010 is used. The emissions from agricultural waste burning and large scale biomass-burning were removed, because it overlaps with fire emissions described later. The latest version of the EDGAR inventory contains the longest time series, which is an advantage for our long-term simulation described in a follow up study (Tsuruta *et al.*, 2016). To be consistent, we applied this version of EDGAR inventory data also in this study. We did not introduce monthly variations in the yearly prior anthropogenic emissions.

Biosphere emissions, dominated by wetlands, are estimated to contribute about 40% of the total CH_4 emissions, where inter-annual variability of emissions from wetland ecosystems is estimated to be 12 Tg CH_4 yr^{-1} (Spahni *et al.*, 2011). For the monthly mean biosphere emissions, the estimates from two biogeochemical process models, LPX-Bern 1.0 (Spahni *et al.*, 2013) and the LPJ-WHyME vegetation model (Spahni *et al.*, 2011), were used to test the impacts of the prior emissions on the results. The emissions from rice fields were removed from both estimates since they were already included in the anthropogenic emissions. EDGARv4.2 FT2010 estimates of the emissions from rice fields were about 13 Tg CH_4 yr^{-1} smaller than that of LPJ-WHyME and LPX-Bern estimates; no scaling was applied to the rice field emissions from the EDGARv4.2 FT2010 estimates.

Methane emission from fire, termites and ocean accounts for only about 20% of the global estimates in total (Kirschke *et al.*, 2013). However, their temporal and spatial variability are large and should be accounted for in the model. Inter-annual variability of emission from fire can be large because of occasional intense fire years, and events such as strong El Niño conditions that lead to dry periods around the Equator (Langenfelds *et al.*, 2002). Also, seasonal and spatial patterns of fire vary due to e.g. vegetation types, changing synoptic weather patterns, agricultural practices, and deforestation (van der Werf *et al.*, 2010). The habitat of termites depends on vegetation types, and the amount of methane emitted from termites depends on the species (Eggleton and Tayasu, 2001).

For fire emissions, monthly mean estimates from the Global Fire Emissions Database version 3.1 (GFEDv3.1) (van der Werf *et al.*, 2010) were used. For termites emission, annual mean estimates from Ito *et al.* (2012) were used. For ocean emissions, monthly mean estimates were calculated as the product of the difference between air and seawater partial pressures of methane (Lambert and Schmidt, 1993), gas transfer velocity, gas solubility. ECMWF ERA-Interim sea surface temperature, sea ice mask, surface pressure and wind speed (Dee *et al.*, 2011) was used for calculating solubility and transfer velocity. The saturation of methane in the surface seawater was assumed to be constant globally and throughout the months.

Geosci. Model Dev. Discuss., doi:10.5194/gmd-2016-181, 2016
Manuscript under review for journal Geosci. Model Dev.
Published: 19 August 2016
© Author(s) 2016. CC-BY 3.0 License.

2.4 Atmospheric methane observations

Atmospheric observations of CH_4 dry-air mole fractions, gathered by a large community of dedicated experimentalists worldwide and made available from the World Data Centre for Greenhouse Gases (WDCGG), were assimilated in CTE-CH_4. The set of observations consists of discrete air sample and continuous measurements from several cooperative networks (Table 1). Observations capturing 'background' signatures of atmospheric CH_4 were selected, and CH_4 values suspected to have strong local influences were excluded using information provided by the experimentalists who conducted the original quality control on their data. For continuous observations, daytime (12-16 local time) observations were selected, except for the high altitude sites (PRS, CMN, SCH, PUY, IZO, JFJ, MLO, ZUG, ZSF) for which night time (0-4 local time) observations were selected. These choices of sampling times reflect a preference for well-mixed conditions that represent large source areas, and are also better captured by the TM5 transport model. No day-night selection was applied to discrete observations. For each site, model-data-mismatches (mdm), used in the observation covariance matrix, were defined based on uncertainty in the observations and the transport model and are given in Table 1. This includes both the observation error and the transport model error, i.e. ability of the transport model to simulate the observations. Note that the latter error is often much larger than the former. For the marine boundary layer and the deep southern hemispheric sites, mdm was set 7.5 ppb, for the sites which captures both land and ocean signals, mdm was set 15 ppb, for the sites capturing signals from land, mdm was set 25 ppb, for the sites with large variation in observations due to local influences, mdm was set 30 ppb, and for the sites appeared problematic in the inversions, mdm was set 75 ppb. During assimilation, rejection thresholds were set as three times mdm.

3. Experiments set-ups

In this study, inversions were performed for a test period between 29 May 2007 and 30 Oct. 2007. Summer was chosen because it is the time when the biospheric CH_4 emissions are largest in the northern hemisphere, and our focus is on the northern boreal region and Europe.

3.1 EnKF parameters' sensitivity experiments

Two EnKF parameters (ensemble size and prior covariance matrix) were assessed using the baseline model, M1, with only discrete air sample observations assimilated, and prior biosphere emission estimates from the LPX-Bern (S3). EnKF has a property that a full posterior probability density function of the state (scaling factor in our case) can be exactly represented by an infinite ensemble of model states. However, computational constraints limit the number of ensemble members. A small number of ensemble members is computationally cheap to apply, but it may lead to a statistical misrepresentation of the posterior distribution. Choosing the suitable number of ensembles is often a question of finding a large enough number of ensembles that is not computationally too expensive. For the sensitivity experiments, we used an ensemble size of 20 (E20) and 500 (E500), and additionally made a specific test for degrees of freedom related to five different ensemble sizes from 20

Geosci. Model Dev. Discuss., doi:10.5194/gmd-2016-181, 2016
Manuscript under review for journal Geosci. Model Dev.
Published: 19 August 2016
© Author(s) 2016. CC-BY 3.0 License.

to 500 (20, 60, 120, 240, 500). FMI has a computer facility with 20 nodes per processor. For E20, one processor is used, and for E500, 13 processors were used. In order to test sensitivities of the prior distribution of the states, we carried out four E20 simulations and three E500 simulations using random initial values sampled from normal distribution with mean 1 and standard deviation 1.

A model error covariance matrix $\boldsymbol{Q}$ is used to create a prior state covariance matrix at the beginning of each time step:

$$\boldsymbol{P}_b^{t+1} = \boldsymbol{P}_a^t + \boldsymbol{Q}, \tag{2}$$

where $\boldsymbol{P}_b^{t+1}$ is the prior state covariance matrix at time $t+1$, and $\boldsymbol{P}_a^t$ is posterior state covariance matrix at time t. Two matrices were examined in this study: identity (**Q1**), and **Q2** which was based on Peters *et al.* (2005):

$$\boldsymbol{Q2} = \begin{pmatrix} \boldsymbol{A}_{IWP} & \boldsymbol{A}^{*1} & \boldsymbol{0} & \boldsymbol{0} & \boldsymbol{0} \\ \boldsymbol{A}^{*1} & \boldsymbol{A}_{WMS} & \boldsymbol{0} & \boldsymbol{0} & \boldsymbol{0} \\ \boldsymbol{0} & \boldsymbol{0} & \boldsymbol{A}_{ANT} & \boldsymbol{A}^{*2} & \boldsymbol{0} \\ \boldsymbol{0} & \boldsymbol{0} & \boldsymbol{A}^{*2} & \boldsymbol{A}_{RIC} & \boldsymbol{0} \\ \boldsymbol{0} & \boldsymbol{0} & \boldsymbol{0} & \boldsymbol{0} & \boldsymbol{\sigma}_{ICE} \end{pmatrix},$$

$$\boldsymbol{A}_{k_{ij}} = \begin{pmatrix} \sigma_k^2 & \sigma_k^2 \cdot e^{-d_{ij}/L} \\ \sigma_k^2 \cdot e^{-d_{ij}/L} & \sigma_k^2 \end{pmatrix} \text{ for } k = \text{IWP, WMS, ANT, RIC.}$$

It is assumed that $\boldsymbol{\lambda}_{\mathrm{IWP}}$, $\boldsymbol{\lambda}_{\mathrm{WMS}}$, $\boldsymbol{\lambda}_{\mathrm{ANT}}$, $\boldsymbol{\lambda}_{\mathrm{RIC}}$, $\boldsymbol{\lambda}_{\mathrm{ICE}}$ are uncorrelated, with each having a variance $\sigma_k^2 = 0.8$. Scaling factors of the same LET regions at different mTC regions (off diagonal of $\boldsymbol{A}_{k_{ij}}$) are assumed to be correlated with $\sigma_k \cdot e^{-d_{ij}/L}$, where d_{ij} is the distance between the centre of the regions (i, j), and the correlation length L = 900km. For mTC3 (south American tropical), 7 (Eurasian boreal), and mTC9 (Asian tropical), between $\boldsymbol{\lambda}_{\mathrm{IWP}}$ and $\boldsymbol{\lambda}_{\mathrm{WMS}}$ ($\boldsymbol{A}^{*1}$), and between $\boldsymbol{\lambda}_{\mathrm{ANT}}$ and $\boldsymbol{\lambda}_{\mathrm{RIC}}$ ($\boldsymbol{A}^{*2}$) are assumed correlated with $\sigma_k^2 \cdot e^{-d_{ij}/L}$ to constrain the emissions in those regions better. The observation network within and around these regions are particularly sparse (only one or no site in the regions), which makes the model difficult to constrain the emissions. For $\boldsymbol{\lambda}_{\mathrm{ICE}}$, variance σ_{ICE}^2 is set to be $1e^{-8}$ for both **Q1** and **Q2**, as the emissions from this region are small, and we assume the prior estimates are already good.

3.2 Other sensitivity experiments

In the following experiments, an ensemble size of 500, the same set of prior state distribution sampled from the same normal distribution with mean 1 and standard deviation 1 (i.e. no random error due to sampling of prior state), and **Q2** covariance were used. In the reference inversion S1, the emissions were estimated using model M1 with an assimilation window length of 5 weeks (i.e. taking into account the observations performed within the corresponding week and the next four ones), with both discrete and continuous methane observations assimilated, using the LPX-Bern emission estimates as the prior biosphere emissions, and the Tiedtke (1989) convection scheme in the TM5 transport model. For sensitivity analysis, seven inversions were performed (Table 2). S2 examines the effects of prior biosphere emissions by replacing the LPX-Bern emissions with the LPJ-WHyME emission estimates. S3 examines the effects of using continuous observations by

Geosci. Model Dev. Discuss., doi:10.5194/gmd-2016-181, 2016
Manuscript under review for journal Geosci. Model Dev.
Published: 19 August 2016
© Author(s) 2016. CC-BY 3.0 License.

assimilating only discrete observations, and S4 examines effects of the assimilation window length by increasing it to 12 weeks instead of 5 weeks. Additionally, the inversions using the M2 model examine effects of increasing the number of scaling factors and simultaneously optimising two scaling factors per region in the model structure (S5). Finally, S6 and S7 examines the effect of the updated convection scheme in TM5 using M1 and M2, respectively.

4. Results

4.2 Sensitivity of EnKF parameters

The results from sensitivity runs (E20-E500) show that the larger the ensemble size, the more stable the results are. With an ensemble size of 500, the mean estimates for the sum of the biosphere and anthropogenic emissions aggregated over the test period only differed by less than 0.5 Tg CH_4 between the three E500 runs (217.9 ± 28.2, 217.7 ± 28.2, 217.4 ± 27.3 Tg CH_4 per test period). However, with ensemble size 20, the mean estimates for the aggregated sum of the biosphere and anthropogenic emissions differed by about 10 Tg CH_4 (216.7 ± 25.3, 221.0 ± 24.9, 224.4 ± 24.3, 225.1 ± 24.6 Tg CH_4). The smaller posterior uncertainties in the E20 experiments than in the E500 experiments are the underestimation of the uncertainties due to the small ensemble size. The weekly sums also show that there are more random variations in the estimates from the E20 experiments compared to the E500 experiments (Fig. 2). These differences depend on the available observations. Regions with dense observational networks, e.g. north American boreal, show less variation in the estimates than where the observation network is sparse, e.g. Asian tropical. This holds for both E20 and E500. The degree of freedom (d.o.f.) in the posterior ensembles (square of sum of singular values divided by sum of square of singular values) is small when the ensemble size is small as we cannot represent more d.o.f. than we have in the ensemble members. It increases significantly until an ensemble size of 120, meaning the information added to the singular value decomposition matrix is significant, but the rate of increase slows down after that, reaching to an equilibrium (Fig. 3). Although we did not test larger ensemble sizes, the results suggest that 500 is large enough to represent the probability distribution well, and will be used in the follow-up experiments.

The computational costs were higher for E500, as expected. With 13 processors of our computational system at FMI, the computational burden was about one hour of wall clock time per week of model time for E500. For E20, the burden was only about half an hour per week of model time with one processor. Note that the computational time of E500 could be as small as E20 if number of nodes is increased to 500, i.e. using 25 processors in case of FMI system. The observation operator was the most expensive, consuming about 80% of computational time for both cases.

The experiments using ***Q1*** and ***Q2*** prior covariance showed that the mean posterior emissions did not differ very much. The posterior emissions using ***Q1*** were 91 ± 14 Tg CH_4 for biosphere emissions and 126 ± 27 Tg CH_4 for anthropogenic emissions (the numbers are aggregated over the entire run of 154 days). The estimates using ***Q2*** were 91 ± 13 Tg CH_4 for the

Geosci. Model Dev. Discuss., doi:10.5194/gmd-2016-181, 2016
Manuscript under review for journal Geosci. Model Dev.
Published: 19 August 2016
© Author(s) 2016. CC-BY 3.0 License.

biosphere and 127 ± 26 Tg CH_4 for the anthropogenic emissions (see also S3 in Table 4). Thus, the differences in the global total posterior uncertainty estimates were small: about 1 Tg CH_4 for both biosphere and anthropogenic emissions. However, the regional uncertainty estimates were clearly lower using ***Q2*** than ***Q1***, especially in the Eurasian boreal and Asian tropical regions, showing the effect of correlations between near-by regions and within the region (Fig. 4). The uncertainty reduction in those areas are important, and the experiment showed the advantage of using the more informative covariance matrix, in which logical choices for spatial error correlations are made.

4.2 Other sensitivity experiments

4.2.1 Reference inversion (S1)

Global total prior biosphere and anthropogenic emissions from inversion S1 over the test period were estimated to be 95 ± 15 Tg CH_4 and 142 ± 40 Tg CH_4 (P1, Table 3). Posterior estimates CH_4 for biosphere and anthropogenic emissions were 82 ± 11 Tg CH_4, and 128 ± 14 Tg, respectively (S1 in Table 4). CTE-CH_4 successfully reduced the prior uncertainties by about 25% for the biosphere and 65% for the anthropogenic emissions. Note that the ocean, fire and termites emissions are also not optimized, but the anthropogenic emissions over the ocean, e.g. from ship and aircraft, were optimized (only one scaling factor for the whole ocean).

Prior and posterior atmospheric methane mole fractions, estimated by the TM5 transport model using prior and posterior emissions, are compared at the site locations and sampling times of the assimilated observations (Fig. 5). The comparisons show that the posterior mole fractions match the observations consistently better throughout the test period, and no strong bias in the north-south gradient is found. As expected, differences between the observations and the estimated mole fractions are smaller in the posterior than the prior, which confirms the ability of CTE-CH_4 under scenario S1 to adjust emission estimates to yield a better match to the observations. S1 is the benchmark for the tests below.

Regional posterior mean anthropogenic and biosphere emissions have weak to moderate correlation (<0.7), resulted in total uncertainty being much smaller than the squared sum of the individual ones. Moderate correlation was found in south American temperate (mTC4), south Africa (mTC6), Australia (mTC10), south west Europe (mTC12) and north east Europe (mTC13). Most of those regions are limited in number of observations within the region, but have influence of the observations nearby.

4.2.2 Effects of prior biosphere emission estimates (S2)

Inversion S2 using a different set of prior biosphere emissions (LPJ-WHyME) gave a global sum of posterior biosphere and anthropogenic emissions of 206 ± 16 Tg CH_4, which is similar to the results from S1 (210 ± 16 Tg CH_4). However, posterior global total biosphere emission was the smallest among all inversions (Fig. 6). Mean biosphere emissions in Asian temperate

Geosci. Model Dev. Discuss., doi:10.5194/gmd-2016-181, 2016
Manuscript under review for journal Geosci. Model Dev.
Published: 19 August 2016
© Author(s) 2016. CC-BY 3.0 License.

and Asian tropical in LPJ-WHyME were smaller than in LPX-Bern, and the posterior emissions were similar to the prior, resulting in smaller posterior mean biosphere emissions in those regions compared to S1 (Fig. 6). However, the estimated sum of the posterior mean biosphere and anthropogenic emissions in those regions were similar to S1, which means that the posterior mean anthropogenic emissions in those regions were larger than in S1. In contrast, the LPJ-WHyME estimates in Eurasian boreal region was much larger than in LPX-Bern. The estimate was reduced in the posterior, but remained about 2 Tg CH_4 larger than the S1 posterior. Similarly, the LPJ-WHyME estimate in northern Europe was about three times larger compared to LPX-Bern. However, the differences in the posterior estimates was only about 0.3 Tg CH_4. This confirms that for northern Europe, our system makes consistent adjustments to fluxes based on observations, and independent of the prior flux magnitude. For Eurasian boreal region, additional observations would help further constrain the estimates.

Uncertainty estimates in S2 for the anthropogenic emissions were similar to S1 in both the prior and posterior, but the prior uncertainty for the biosphere emissions were slightly larger in S2 than in S1. The largest differences were found in north west Europe; both prior and posterior uncertainties for the biosphere emissions were only 1 Tg CH_4 in S1, but the S2 prior and posterior uncertainty estimates were 6 Tg CH_4 and 2 Tg CH_4, respectively. Similarly, the S2 prior uncertainties in Eurasian boreal were more than three times larger than those in S1. However, for both regions, the differences in the posterior uncertainties were smaller: 1 Tg CH_4 for north west Europe, and 2 Tg CH_4 for Eurasian boreal. On the other hand, the S2 uncertainty for biosphere emissions in Asian temperate and Asian tropical were 1~3 Tg CH_4 smaller than those of S1 in both the prior and posterior. Therefore, for further analysis in the accompanying paper, we continue to use LPX-Bern estimates as the prior for biospheric emissions as our focus is more on northern boreal regions than on Asia.

4.2.3 Effects of continuous observations (S3)

Global total posterior mean anthropogenic emission in inversion S3 was similar to S1. However, in regions where many continuous observations are available, e.g. north American temperate and south west and east Europe, the posterior mean anthropogenic emissions were about 70% smaller in S3 compared to S1. On the other hand, regions where not many continuous observations are available in and around the regions, such as south America, Eurasian boreal and Australia, the differences in the emission estimates were small. This is expected, as the number of observations stays the same as in S1, and the assumptions in prior error covariance matrix (Section 3.1) allow little influence from regions further away. Similarly for the posterior mean biosphere emissions, the largest differences are seen in the north American temperate region, where many continuous observations are available; the difference is smaller in northern American boreal region, and larger in the temperate region (Fig. 6). The global total posterior mean biosphere emission was the largest among all the inversions (Table 4). Furthermore, differences in the estimates in Asian tropics were large, although the observation network is already sparse in this region in S1. The flux estimates and their interpretation using this set up will be presented in the companion paper (Tsuruta *et al.*, 2016).

Geosci. Model Dev. Discuss., doi:10.5194/gmd-2016-181, 2016
Manuscript under review for journal Geosci. Model Dev.
Published: 19 August 2016
© Author(s) 2016. CC-BY 3.0 License.

The differences in the posterior uncertainty estimates were larger in the anthropogenic emissions than in the biosphere emissions. The posterior uncertainty for the global anthropogenic emissions was about two times larger in S3 compared to S1. This effect was also clearly seen in the regional estimates; the S3 anthropogenic uncertainty estimates were twice or larger than S1 in the north American temperate and Asian temperate regions, and south west Europe. Although the S3 and S1 uncertainty estimates for the biosphere emissions did not differ much for the global total emission, clear differences were seen in some regions; the S3 biosphere uncertainty estimates were about three times higher in north American boreal, and about twice larger in Asian temperate, and about 20% larger in the north American temperate, Eurasian boreal and Asian tropical regions than those in the S1 estimates.

4.2.4 Effects of assimilation window size (S4)

Using the longer assimilation window length, CTE-CH_4 assimilates observations of further distances in time, which could be an advantage in regions where the observation network is sparse. However, the longer travel time between sources and observations also increases the transport error, and correlates the transport errors across the observation network making them less informative. Despite that, the mean and uncertainty estimates in S4 were close to S1 for both anthropogenic and biosphere emissions, and we did not see the expected differences in regions such as the tropics (see also Babenhauserheide *et al.*, 2016). The posterior mean biosphere emissions in north American boreal and south American tropical are slightly lower, and the estimates in the north American temperate and Asian tropical regions are slightly higher compared to S1. No significant differences were found in uncertainty estimates.

4.2.5. Effects of simultaneously optimizing two scaling factors (S5)

Posterior mean biosphere and anthropogenic emissions in inversion S5 were very similar to S1 (Table 4). However, for Eurasian boreal, Asian temperate and Asian tropical, ratio of the posterior mean biosphere emissions (E_{bio}) to the anthropogenic emissions (E_{anth}) were very different from S1. The ratio E_{bio}/E_{anth} in those regions are 0.63, 1.14, 0.98 for S1, and 1.12, 0.76, 1.85 for S5, respectively. This shows that the dominating emissions (either biosphere or anthropogenic) in those regions are opposite in S1 and S5. Other noticeable differences were found in the north American temperate region and northern Europe (east and west). In north American temperate and north west Europe, the S5 posterior mean anthropogenic emissions were about 15% and about 30% smaller than S1, respectively, and in north east Europe, the anthropogenic emission was about 20% larger than in S1.

Generally, the posterior uncertainties were larger in S5 than in S1. This is expected; each region carries either biosphere or anthropogenic emission uncertainty in M1, but every grid carries both biosphere and anthropogenic emission uncertainties in M2. The mean uncertainty estimates were generally similar (not shown). However in some regions, such as Asian temperate and tropical, and Eurasian boreal, the S5 uncertainties were more than a double. On the other hand, the uncertainty estimate for south west Europe was nearly half of S1 estimate. Posterior mean anthropogenic emission over the ocean and its

Geosci. Model Dev. Discuss., doi:10.5194/gmd-2016-181, 2016
Manuscript under review for journal Geosci. Model Dev.
Published: 19 August 2016
© Author(s) 2016. CC-BY 3.0 License.

uncertainty did not change much from the prior in S5 because the prior uncertainty of the scaling factor was unintentionally set very small ($\sigma^2 = 1e^{-8}$). However, when it is corrected, we expect the estimate and uncertainty to be similar to that of S7, in which the prior uncertainty was set to 0.8.

4.3.6 Effects of TM5 convection scheme (S6, S7)

Global total posterior mean global biosphere and anthropogenic emissions in S6 and S7 inversions showed that the estimates using either the Tiedtke (1989) or Gregory *et al.* (2000) convection scheme were similar. However, the sum of the posterior mean emissions in the southern hemisphere is slightly smaller, and that in the northern hemisphere is larger when the Gregory *et al.* (2000) convection scheme is used. Due to faster vertical mixing in the northern hemisphere in the Gregory *et al.* (2000) convection scheme, the simulated atmospheric methane mole fractions in the troposphere became lower compared to using the Tiedtke (1989) convection scheme. Therefore, CTE-CH_4 produces higher emission estimates in the northern hemisphere when the Gregory *et al.* (2000) convection scheme is used. This feature was seen in both S6 and S7. In both inversions, the uncertainty estimates were not significantly different from inversions using the Tiedtke (1989) convection scheme (S1 and S5).

Changes in convection schemes lead to large differences in posterior flux estimates. The effect of convection was generally larger when using M2 than M1. For anthropogenic emissions, the M1 and M2 differed by the number of mTC regions affected by the convection schemes. Using M2 (S7 compared to S5), posterior anthropogenic emissions differed by more than 10% in 12 mTC regions due to convection, whereas using M1 (S6 compared to S1), the posterior anthropogenic emissions differed by more than 10% only in two mTC regions. For biosphere emissions, the number of regions affected were similar in both models, but the differences in the estimates was generally larger in M2. The extreme cases were seen in Asian temperate and north west Europe. In M2, posterior mean biosphere emissions in Asian temperate using Gregory *et al*. (2000) was more than 130% smaller than those using Tiedtke (1989), and posterior mean anthropogenic emission in north west Europe was about 45% larger when using Gregory *et al*. (2000) than using Tiedtke (1989), but the estimates differed only by about 1% and 8% in M1 in those regions, respectively. These results show that larger differences in the posterior estimates were derived from the changes in the convection schemes using M2 (S5 and S7) than using M1 (S1 and S6).

4.3 Atmospheric mole fractions

For the S1-S7 inversions, the prior and posterior methane mole fractions were calculated with TM5 using the prior and posterior emissions respectively, respectively. For the inversions S1-S5, the Tiedtke (1989) convection scheme was used, and for the inversions S6-S7, Gregory *et al.* (2000) was used; same the convection schemes used in inversion and forward mode. For the inversions, NOAA discrete air sample observations were compared to modelled mole fractions and summarized in a Taylor diagram (Taylor, 2001) (Fig. 7). Globally, agreement with the observations did not differ much between the inversions (Fig. 7, top), meaning that the CTE-CH4 successfully optimized emissions consistent with the

Geosci. Model Dev. Discuss., doi:10.5194/gmd-2016-181, 2016
Manuscript under review for journal Geosci. Model Dev.
Published: 19 August 2016
© Author(s) 2016. CC-BY 3.0 License.

observations globally on average regardless of the setups. However, for European sites, S3 posterior mole fractions matched the observations best, and poorest in S7 (Fig. 7, bottom left). In other words, the additional information from the continuous observations was useful in gaining better agreement with NOAA observations. For both global and Europe, variability in the posterior mole fractions were lower than in the observed mole fractions. For Asian temperate, the S6 and S7 posterior estimates matched the observations noticeably better than the other inversions (Fig. 7, bottom right). This suggests that using the Gregory *et al.* (2000) convection scheme in TM5 gives a better match to the observations in that region.

5 Discussion

The reference inversion (S1) successfully reduced the uncertainty of the emission estimates, and its posterior mole fractions showed good agreement with observations globally. The global total uncertainty estimate was one of the smallest among all inversions, although uncertainty for the global anthropogenic emissions was the smallest in S2. The comparison between the posterior mole fractions and the observations was among the best in all mTC regions (not shown). Although the best way to interpret performance of the inversions are to compare with independent observations not assimilated in the inversion, this suggests that S1 has an optimal set-up within the seven inversions tested in this study.

The S2 inversion showed that CTE-CH_4 relies on the prior emissions of the biosphere to some extent, and the posterior emissions are forced to compensate for strongly differing prior biosphere emissions by changing the anthropogenic component. For the Eurasian boreal and Asian tropical regions, the influence of the prior estimates were large mostly due to the limited number of observations available to separately constrain both components. For the Asian temperate region, the reason could be that under large influence of anthropogenic emissions, and the discrete observations may have little effect on the biosphere emissions. If the discrete observations are located nearer to the anthropogenic sources, it could takes longer to have influence on the biosphere emissions. For Asian tropical and temperate regions, effect of the discrete observations could be higher if longer assimilation window is used or inversion period is extended.

The S3 inversion showed that increasing the number of observations does not necessary help to reduce uncertainties. Indeed, the additional observation uncertainty increased the emission uncertainty also. The impact on the S3 uncertainty estimates was larger for the anthropogenic emissions than for the biosphere emissions. One of the reasons for this is that there are more continuous observations in the regions where anthropogenic emissions dominate: namely northern America, Asian temperate and southern Europe. However, the agreement with the NOAA discrete observations, assimilated in both S3 and S1, was better in S3 than in S1 (Fig. 7). This could imply that the estimated uncertainty using only discrete observations may be underestimated. In this study, we only assessed the effect of adding continuous observations, but different effect could be seen if e.g. different set of discrete observations were used.

Geosci. Model Dev. Discuss., doi:10.5194/gmd-2016-181, 2016
Manuscript under review for journal Geosci. Model Dev.
Published: 19 August 2016
© Author(s) 2016. CC-BY 3.0 License.

The S4 inversion shows that the assimilation window length does not have a large impact on both the mean and the uncertainty estimates. Although longer assimilation window lengths have been used in Bruhwiler *et al.* (2005), it seems the parameter has only minor influence in our study. One of the reasons would be the short test period we analyzed here, as the correlation between tropical and extratropical fluxes becomes significant only after several months of transport time scales when using long assimilation window lengths. Simulations with longer time periods may reveal the impacts also in our model, especially in the tropics, but it may have negative influence in other regions (Babenhauserheide *et al.*, 2015).

The comparison between S1 and S5 showed that the ratio of the posterior biosphere and anthropogenic emissions varies, and the posterior anthropogenic emissions in the northern latitudes can differ more than 15%. The differences can be partly explained by the proportion of anthropogenic and biosphere land. If we define $r_{land} = N_{bioland}/N_{anthland}$, where $N_{bioland}$ and $N_{anthland}$ are the number of biosphere (IWP & WMS) and anthropogenic (RIC & ANT) grids in 1x1 land ecosystem region, respectively. The ratio r_{land} is larger than 1, i.e. biosphere regions dominate, in Asian tropical, and north west and east Europe, although anthropogenic emissions are of large significance there. This has implications in S1, where only the dominant land use type is considered. In those regions, the differences between the prior and posterior anthropogenic emissions were larger in S5 than in S1. Similarly, r_{land} is smaller than 1, i.e. anthropogenic region dominates, in Eurasian boreal, Asian temperate, northern American boreal and northern American temperate. In those regions, the differences between the prior and posterior biosphere emissions were larger in S5 than in S1. Both cases can be explained by the increase in r_{land} in S5, where the ratio is exactly 1 in all mTC regions. However, the estimates in S5 may be larger or smaller than in S1, which is likely to depend on the observations.

The S6 and S7 inversions showed that CTE-CH_4 resulted in higher emissions in the northern hemisphere when the Gregory *et al.* (2000) convection scheme was used. The comparison between the modelled and observed atmospheric methane mole fractions showed that the posterior mole fractions matched better when using the Tiedtke (1989) convection scheme than when using the Gregory *et al.* (2000) scheme in north American temperate and southern Europe. However, for Asia and high northern latitudes (northern American boreal and northern Europe), the posterior mole fractions matched the observations better when using Gregory *et al.* (2000). For the southern hemispheric mTC regions the differences were not clear mainly due to the small amount of observations on land. Furthermore, the effect of convection was larger in M2 than in M1. One of the reasons is the increase in the $r_{anthland}$ or $r_{bioland}$. If a large prior biosphere emission remains in "anthropogenic regions" (RIC, ANT, WTR), the effect of convection in biosphere emission estimates in M2 would be larger than in M1 because biosphere emissions in those regions are not optimized in M1. This was the case for the Asian temperate region; the sum of prior biosphere emissions in anthropogenic regions was about 20 Tg CH_4 (nearly 75% of the regional prior biosphere emissions). Similarly for north west Europe, the prior anthropogenic emissions in biosphere regions (IWP, WMS) was about 74% of the regional total prior anthropogenic emissions. In other words, M2 is more influenced by strong vertical convection than M1 because both anthropogenic and biosphere emissions are optimised for all regions in M2.

Geosci. Model Dev. Discuss., doi:10.5194/gmd-2016-181, 2016
Manuscript under review for journal Geosci. Model Dev.
Published: 19 August 2016
© Author(s) 2016. CC-BY 3.0 License.

6 Conclusions

This study presented the CTE-CH_4 inverse model together with the impacts of changes in its parameters and inputs. The presented analysis shows that the results were stable with 500 ensemble size, and an informative covariance is useful for the uncertainty reduction. It has been known that the spatial distribution in the prior estimates are important to the models that optimize the fluxes region-wise, and this study confirmed once again that the prior estimates also have an effect on the regional total estimates. Especially for regions with a sparse observation network, such as Eurasian boreal, the posterior estimates stayed close to the prior. Thus, improving the prior estimates is important even when using an inverse model in the absence of observations. Moreover, the importance of the observations was addressed in this study. Using continuous observations, the agreement with NOAA discrete observations improved than using discrete observations alone. The uncertainty estimates were higher when continuous observations were assimilated, due to higher variability in the continuous observations. This suggests that estimated uncertainty using only discrete observations may be underestimated. The effects of the assimilation window length were not large in this study, which needs further assessment using a longer time period. Increasing the number of scaling factors and simultaneously optimizing both anthropogenic and biosphere emission estimates showed that the larger the area or emission is, the larger the differences are between the prior and the posterior estimates. Finally, our study showed that the convection scheme in the TM5 has impact on the north-south gradient of the emission estimates. CTE-CH_4 using the Tiedtke (1998) convection scheme resulted in about 10 Tg CH_4 larger emissions in the northern hemisphere than the model using the Gregory *et al.* (2000) convection scheme. The effect of convection also depended on the definition of land cover map and emission types associated to it. The effect of the convection scheme over a longer time period will be assessed in an accompanying paper.

All parameters and inputs influence the model to a certain degree, but we address the importance of using a large enough ensemble size, informative prior error covariance, good prior emission estimates, sufficient observations, definition of the regions, and the choice of convection schemes in the transport model. We choose CTE-CH_4 with S1 settings (version 1.0), and S5 settings (version 1.1) for our follow up study covering a longer time period. Further analysis of these long-term simulations using both versions continues in the second part of this paper.

Code and data availability

The source code of CTE-CH_4 and data presented in this paper will be provided on request from the corresponding author (Aki Tsuruta: Aki.Tsuruta@fmi.fi).

Acknowledgements. We thank the NCoE DEFROST, NCoE eSTICC and the Finnish Academy project CARB-ARC (285630) for their financial support. We thank Dr. Akihiko Ito for providing prior emissions of termites. We are grateful for the National Oceanic and

© Author(s) 2016. CC-BY 3.0 License.

Atmospheric Administration, Earth System Research Laboratory (NOAA/ESRL), Swiss Federal Laboratories for Materials Science and Technology (EMPA), Environment Canada (EC), Laboratoire des Sciences du Climat et de l'Environnement (LSCE), the National Institute of Water and Atmospheric Research Ltd. (NIWA), the Japan Meteorological Agency (JMA), National Institute for Environmental Studies (NIES), Umweltbundesamt (UBA, Federal Environmental Agency) Air Monitoring Network, Izana Atmospheric Research Center, Meteorological State Agency of Spain (AEMET), the South African Weather Service (SAWS), the Main Geophysical Observatory (MGO), the Korea Meteorological Administration (KMA), National Institute of Environmental Research (NIER), National Institute of Public Health and the Environment (RIVM) for performing high-quality CH4 measurements at global sites and making them available through the GAW-WDCGG.

References

Alexe, M., Bergamaschi, P., Segers, A., Detmers, R., Butz, A., Hasekamp, O., Guerlet, S., Parker, R., Boesch, H., Frankenberg, C., Scheepmaker, R. A., Dlugokencky, E., Sweeney, C., Wofsy, S. C. and Kort, E. A.: Inverse modelling of CH_4 emissions for 2010–2011 using different satellite retrieval products from GOSAT and SCIAMACHY, Atmos. Chem. Phys., 15(1), 113–133, doi:10.5194/acp-15-113-2015, 2015.

Babenhauserheide, A., Basu, S., Houweling, S., Peters, W. and Butz, A.: Comparing the CarbonTracker and TM5-4DVar data assimilation systems for CO2 surface flux inversions, Atmos. Chem. Phys., 15(17), 9747–9763, doi:10.5194/acp-15-9747-2015, 2015.

Beck, V., Chen, H., Gerbig, C., Bergamaschi, P., Bruhwiler, L., Houweling, S., Röckmann, T., Kolle, O., Steinbach, J., Koch, T., Sapart, C. J., van der Veen, C., Frankenberg, C., Andreae, M. O., Artaxo, P., Longo, K. M. and Wofsy, S. C.: Methane airborne measurements and comparison to global models during BARCA, J. Geophys. Res., 117(D15), doi:10.1029/2011JD017345, 2012.

Bergamaschi, P., Krol, M., Dentener, F., Vermeulen, A., Meinhardt, F., Graul, R., Ramonet, M., Peters, W. and Dlugokencky, E. J.: Inverse modelling of national and European CH_4 emissions using the atmospheric zoom model TM5, Atmos. Chem. Phys., 5(9), 2431–2460, doi:10.5194/acp-5-2431-2005, 2005.

Bergamaschi, P., Frankenberg, C., Meirink, J. F., Krol, M., Villani, M. G., Houweling, S., Dentener, F., Dlugokencky, E. J., Miller, J. B., Gatti, L. V., Engel, A. and Levin, I.: Inverse modeling of global and regional CH_4 emissions using SCIAMACHY satellite retrievals, J. Geophys. Res., 114(D22), D22301, doi:10.1029/2009JD012287, 2009.

Bergamaschi, P., Krol, M., Meirink, J. F., Dentener, F., Segers, A., van Aardenne, J., Monni, S., Vermeulen, A. T., Schmidt, M., Ramonet, M., Yver, C., Meinhardt, F., Nisbet, E. G., Fisher, R. E., O'Doherty, S. and Dlugokencky, E. J.: Inverse modeling of European CH_4 emissions 2001–2006, J. Geophys. Res., 115(D22), D22309, doi:10.1029/2010JD014180, 2010.

Bergamaschi, P., Houweling, S., Segers, A., Krol, M., Frankenberg, C., Scheepmaker, R. A., Dlugokencky, E., Wofsy, S. C., Kort, E. A., Sweeney, C., Schuck, T., Brenninkmeijer, C., Chen, H., Beck, V. and Gerbig, C.: Atmospheric CH_4 in the first

© Author(s) 2016. CC-BY 3.0 License.

decade of the 21st century: Inverse modeling analysis using SCIAMACHY satellite retrievals and NOAA surface measurements, J. Geophys. Res. Atmos., 118(13), 7350–7369, doi:10.1002/jgrd.50480, 2013.

Bergamaschi, P., Corazza, M., Karstens, U., Athanassiadou, M., Thompson, R. L., Pison, I., Manning, A. J., Bousquet, P., Segers, A., Vermeulen, A. T., Janssens-Maenhout, G., Schmidt, M., Ramonet, M., Meinhardt, F., Aalto, T., Haszpra, L., Moncrieff, J., Popa, M. E., Lowry, D., Steinbacher, M., Jordan, A., O'Doherty, S., Piacentino, S. and Dlugokencky, E.: Top-down estimates of European CH_4 and N2O emissions based on four different inverse models, Atmos. Chem. Phys., 15(2), 715–736, doi:10.5194/acp-15-715-2015, 2015.

Bousquet, P., Ciais, P., Miller, J. B., Dlugokencky, E. J., Hauglustaine, D. A., Prigent, C., Van der Werf, G. R., Peylin, P., Brunke, E.-G., Carouge, C., Langenfelds, R. L., Lathière, J., Papa, F., Ramonet, M., Schmidt, M., Steele, L. P., Tyler, S. C. and White, J.: Contribution of anthropogenic and natural sources to atmospheric methane variability, Nature, 443(7110), 439–443, doi:10.1038/nature05132, 2006.

Bousquet, P., Ringeval, B., Pison, I., Dlugokencky, E. J., Brunke, E.-G., Carouge, C., Chevallier, F., Fortems-Cheiney, A., Frankenberg, C., Hauglustaine, D. A., Krummel, P. B., Langenfelds, R. L., Ramonet, M., Schmidt, M., Steele, L. P., Szopa, S., Yver, C., Viovy, N. and Ciais, P.: Source attribution of the changes in atmospheric methane for 2006–2008, Atmos. Chem. Phys., 11(8), 3689–3700, doi:10.5194/acp-11-3689-2011, 2011.

Bruhwiler, L., Dlugokencky, E., Masarie, K., Ishizawa, M., Andrews, A., Miller, J., Sweeney, C., Tans, P. and Worthy, D.: CarbonTracker-CH_4: an assimilation system for estimating emissions of atmospheric methane, Atmos. Chem. Phys., 14(16), 8269–8293, doi:10.5194/acp-14-8269-2014, 2014.

Bruhwiler, L. M. P., Michalak, A. M., Peters, W., Baker, D. F. and Tans, P.: An improved Kalman Smoother for atmospheric inversions, Atmos. Chem. Phys., 5(10), 2691–2702, doi:10.5194/acp-5-2691-2005, 2005.

Brühl, C. and Crutzen, P. J.: The MPIC 2D model, in: NASA Ref. Publ. 1292, 1, 103–104, 1993.

Chen, Y.-H. and Prinn, R. G.: Estimation of atmospheric methane emissions between 1996 and 2001 using a three-dimensional global chemical transport model, J. Geophys. Res., 111(D10), D10307, doi:10.1029/2005JD006058, 2006.

Dee, D. P., Uppala, S. M., Simmons, A. J., Berrisford, P., Poli, P., Kobayashi, S., Andrae, U., Balmaseda, M. A., Balsamo, G., Bauer, P., Bechtold, P., Beljaars, A. C. M., van de Berg, L., Bidlot, J., Bormann, N., Delsol, C., Dragani, R., Fuentes, M., Geer, A. J., Haimberger, L., Healy, S. B., Hersbach, H., Hólm, E. V., Isaksen, L., Kållberg, P., Köhler, M., Matricardi, M., McNally, A. P., Monge-Sanz, B. M., Morcrette, J.-J., Park, B.-K., Peubey, C., de Rosnay, P., Tavolato, C., Thépaut, J.-N. and Vitart, F.: The ERA-Interim reanalysis: configuration and performance of the data assimilation system, Q.J.R. Meteorol. Soc., 137(656), 553–597, doi:10.1002/qj.828, 2011.

Eggleton, P. and Tayasu, I.: Feeding groups, lifetypes and the global ecology of termites, Ecol. Res., 16(5), 941–960, 2001.

Evensen, G.: The Ensemble Kalman Filter: theoretical formulation and practical implementation, Ocean Dynam., 53(4), 343–367, doi:10.1007/s10236-003-0036-9, 2003.

Fraser, A., Palmer, P. I., Feng, L., Boesch, H., Cogan, A., Parker, R., Dlugokencky, E. J., Fraser, P. J., Krummel, P. B., Langenfelds, R. L., O'Doherty, S., Prinn, R. G., Steele, L. P., van der Schoot, M. and Weiss, R. F.: Estimating regional

© Author(s) 2016. CC-BY 3.0 License.

methane surface fluxes: the relative importance of surface and GOSAT mole fraction measurements, Atmos. Chem. Phys., 13(11), 5697–5713, doi:10.5194/acp-13-5697-2013, 2013.

Gregory, D., Morcrette, J.-J., Jakob, C., Beljaars, A. C. M. and Stockdale, T.: Revision of convection, radiation and cloud schemes in the ECMWF integrated forecasting system, Q.J.R. Meteorol. Soc., 126(566), 1685–1710, doi:10.1002/qj.49712656607, 2000.

Houweling, S., Krol, M., Bergamaschi, P., Frankenberg, C., Dlugokencky, E. J., Morino, I., Notholt, J., Sherlock, V., Wunch, D., Beck, V., Gerbig, C., Chen, H., Kort, E. A., Röckmann, T. and Aben, I.: A multi-year methane inversion using SCIAMACHY, accounting for systematic errors using TCCON measurements, Atmos. Chem. Phys., 14(8), 3991–4012, doi:10.5194/acp-14-3991-2014, 2014.

Huijnen, V., Williams, J., van Weele, M., van Noije, T., Krol, M., Dentener, F., Segers, A., Houweling, S., Peters, W., de Laat, J., Boersma, F., Bergamaschi, P., van Velthoven, P., Le Sager, P., Eskes, H., Alkemade, F., Scheele, R., Nédélec, P. and Pätz, H.-W.: The global chemistry transport model TM5: description and evaluation of the tropospheric chemistry version 3.0, Geosci. Model Dev., 3(2), 445–473, doi:10.5194/gmd-3-445-2010, 2010.

Ito, A. and Inatomi, M.: Use of a process-based model for assessing the methane budgets of global terrestrial ecosystems and evaluation of uncertainty, Biogeosciences, 9(2), 759–773, doi:10.5194/bg-9-759-2012, 2012.

Kirschke, S., Bousquet, P., Ciais, P., Saunois, M., Canadell, J. G., Dlugokencky, E. J., Bergamaschi, P., Bergmann, D., Blake, D. R., Bruhwiler, L., Cameron-Smith, P., Castaldi, S., Chevallier, F., Feng, L., Fraser, A., Heimann, M., Hodson, E. L., Houweling, S., Josse, B., Fraser, P. J., Krummel, P. B., Lamarque, J.-F., Langenfelds, R. L., Le Quéré, C., Naik, V., O'Doherty, S., Palmer, P. I., Pison, I., Plummer, D., Poulter, B., Prinn, R. G., Rigby, M., Ringeval, B., Santini, M., Schmidt, M., Shindell, D. T., Simpson, I. J., Spahni, R., Steele, L. P., Strode, S. A., Sudo, K., Szopa, S., van der Werf, G. R., Voulgarakis, A., van Weele, M., Weiss, R. F., Williams, J. E. and Zeng, G.: Three decades of global methane sources and sinks, Nature Geosci., 6(10), 813–823, doi:10.1038/ngeo1955, 2013.

Krol, M., Houweling, S., Bregman, B., van den Broek, M., Segers, A., van Velthoven, P., Peters, W., Dentener, F. and Bergamaschi, P.: The two-way nested global chemistry-transport zoom model TM5: algorithm and applications, Atmos. Chem. Phys., 5(2), 417–432, doi:10.5194/acp-5-417-2005, 2005.

Lambert, G. and Schmidt, S.: Proceedings of the NATO advanced research workshop Reevaluation of the oceanic flux of methane: Uncertainties and long term variations, Chemosphere, 26(1), 579–589, doi:10.1016/0045-6535(93)90443-9, 1993.

Langenfelds, R. L., Francey, R. J., Pak, B. C., Steele, L. P., Lloyd, J., Trudinger, C. M. and Allison, C. E.: Interannual growth rate variations of atmospheric CO2 and its δ13C, H2, CH_4, and CO between 1992 and 1999 linked to biomass burning, Global Biogeochem. Cy., 16(3), 1048, doi:10.1029/2001GB001466, 2002.

Locatelli, R., Bousquet, P., Chevallier, F., Fortems-Cheney, A., Szopa, S., Saunois, M., Agusti-Panareda, A., Bergmann, D., Bian, H., Cameron-Smith, P., Chipperfield, M. P., Gloor, E., Houweling, S., Kawa, S. R., Krol, M., Patra, P. K., Prinn, R.

© Author(s) 2016. CC-BY 3.0 License.

G., Rigby, M., Saito, R. and Wilson, C.: Impact of transport model errors on the global and regional methane emissions estimated by inverse modelling, Atmos. Chem. Phys., 13(19), 9917–9937, doi:10.5194/acp-13-9917-2013, 2013.

Olivié, D. J. L., van Velthoven, P. F. J., Beljaars, A. C. M. and Kelder, H. M.: Comparison between archived and off-line diagnosed convective mass fluxes in the chemistry transport model TM3, J. Geophys. Res., 109(D11), D11303, doi:10.1029/2003JD004036, 2004.

Peters, W., Miller, J. B., Whitaker, J., Denning, A. S., Hirsch, A., Krol, M. C., Zupanski, D., Bruhwiler, L. and Tans, P. P.: An ensemble data assimilation system to estimate CO2 surface fluxes from atmospheric trace gas observations, J. Geophys. Res., 110(D24), D24304, doi:10.1029/2005JD006157, 2005.

Pison, I., Bousquet, P., Chevallier, F., Szopa, S. and Hauglustaine, D.: Multi-species inversion of CH_4, CO and H2 emissions from surface measurements, Atmos. Chem. Phys., 9(14), 5281–5297, 2009.

Prigent, C., Papa, F., Aires, F., Rossow, W. B. and Matthews, E.: Global inundation dynamics inferred from multiple satellite observations, 1993–2000, J. Geophys. Res., 112(D12), doi:10.1029/2006JD007847, 2007.

Spahni, R., Wania, R., Neef, L., van Weele, M., Pison, I., Bousquet, P., Frankenberg, C., Foster, P. N., Joos, F., Prentice, I. C. and van Velthoven, P.: Constraining global methane emissions and uptake by ecosystems, Biogeosciences, 8(6), 1643–1665, doi:10.5194/bg-8-1643-2011, 2011.

Spahni, R., Joos, F., Stocker, B. D., Steinacher, M. and Yu, Z. C.: Transient simulations of the carbon and nitrogen dynamics in northern peatlands: from the Last Glacial Maximum to the 21st century, Clim. Past, 9(3), 1287–1308, doi:10.5194/cp-9-1287-2013, 2013.

Spivakovsky, C. M., Logan, J. A., Montzka, S. A., Balkanski, Y. J., Foreman-Fowler, M., Jones, D. B. A., Horowitz, L. W., Fusco, A. C., Brenninkmeijer, C. a. M., Prather, M. J., Wofsy, S. C. and McElroy, M. B.: Three-dimensional climatological distribution of tropospheric OH: Update and evaluation, J. Geophys. Res., 105(D7), 8931–8980, doi:10.1029/1999JD901006, 2000.

Taylor, K. E.: Summarizing multiple aspects of model performance in a single diagram, J. Geophys. Res., 106(D7), 7183–7192, doi:10.1029/2000JD900719, 2001.

Tiedtke, M.: A Comprehensive Mass Flux Scheme for Cumulus Parameterization in Large-Scale Models, Mon. Wea. Rev., 117(8), 1779–1800, doi:10.1175/1520-0493(1989)117<1779:ACMFSF>2.0.CO;2, 1989.

Tsuruta, A., Aalto, T., Backman, L., Peters, W., Krol, M., van der Laan-Luijkx, I. T., Hatakka, J., Heikkinen, P., Dlugokencky, E. J., Spahni, R. and Paramonova, N.: evaluating atmospheric methane inversion model results for Pallas, northern Finland., Boreal Environ. Res., 20(4), 2015.

Tsuruta, A., Aalto, T., Backman, L., Hakkarainen, J., van der Laan-Luijkx, I. T., Peters, W., Krol, M., Spahni, R., Houweling, S., and Laine, M.: Development of CarbonTracker Europe-CH_4 – Part 2: global methane emission estimates and their evaluation for 2000-2012, 2016 (submitted to Geosci. Model Dev. Discuss.)

Wania, R., Ross, I. and Prentice, I. C.: Implementation and evaluation of a new methane model within a dynamic global vegetation model: LPJ-WHyME v1.3.1, Geosci. Model Dev., 3(2), 565–584, doi:10.5194/gmd-3-565-2010, 2010.

Geosci. Model Dev. Discuss., doi:10.5194/gmd-2016-181, 2016
Manuscript under review for journal Geosci. Model Dev.
Published: 19 August 2016
© Author(s) 2016. CC-BY 3.0 License.

van der Werf, G. R., Randerson, J. T., Giglio, L., Collatz, G. J., Mu, M., Kasibhatla, P. S., Morton, D. C., DeFries, R. S., Jin, Y. and van Leeuwen, T. T.: Global fire emissions and the contribution of deforestation, savanna, forest, agricultural, and peat fires (1997–2009), Atmos. Chem. Phys., 10(23), 11707–11735, doi:10.5194/acp-10-11707-2010, 2010.

Geosci. Model Dev. Discuss., doi:10.5194/gmd-2016-181, 2016
Manuscript under review for journal Geosci. Model Dev.
Published: 19 August 2016
© Author(s) 2016. CC-BY 3.0 License.

Geoscientific Model Development Discussions
Open Access

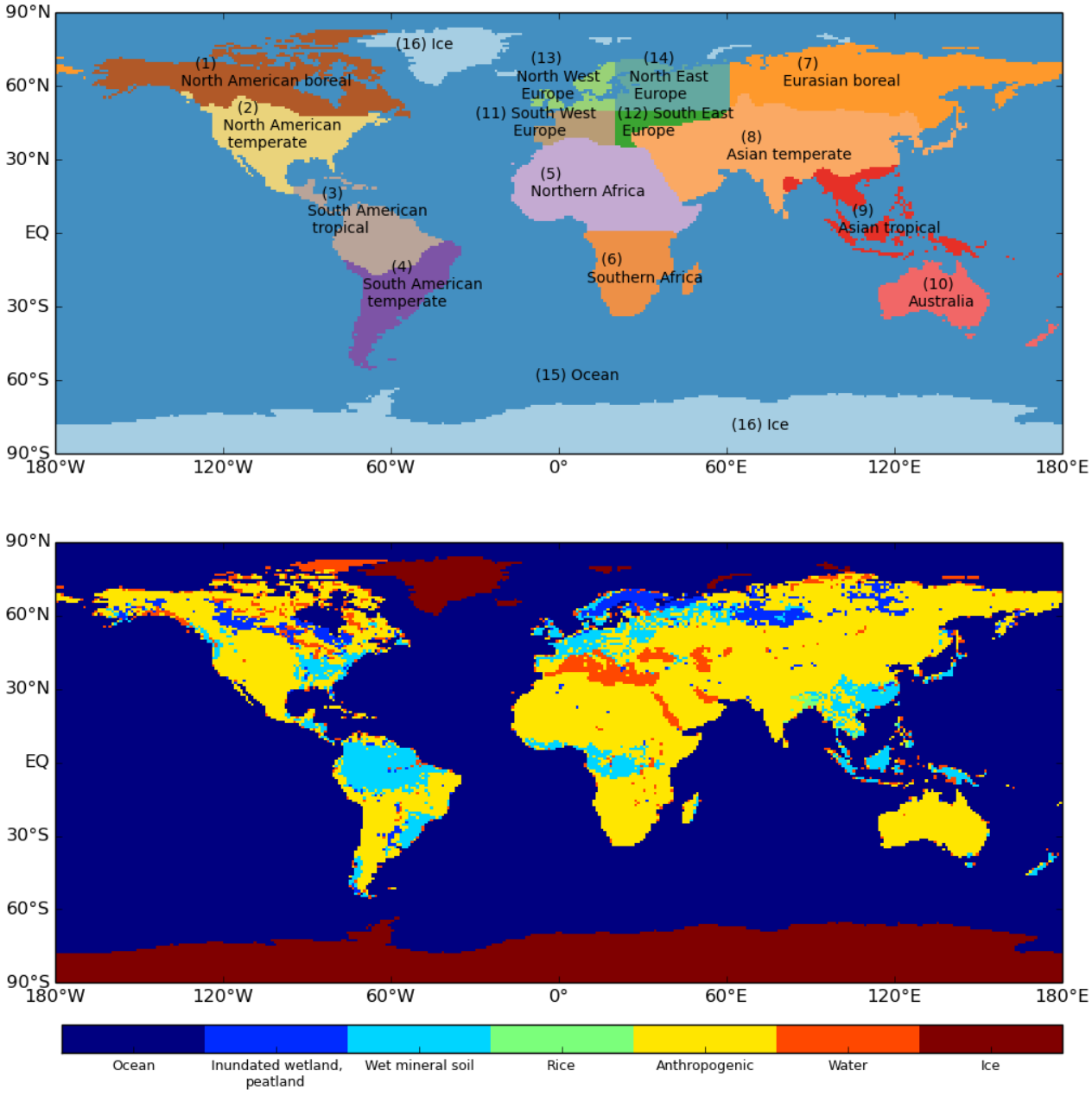

Figure 1: Modified mTC (top) and land ecosystem (bottom) regions.

Geosci. Model Dev. Discuss., doi:10.5194/gmd-2016-181, 2016
Manuscript under review for journal Geosci. Model Dev.
Published: 19 August 2016
© Author(s) 2016. CC-BY 3.0 License.

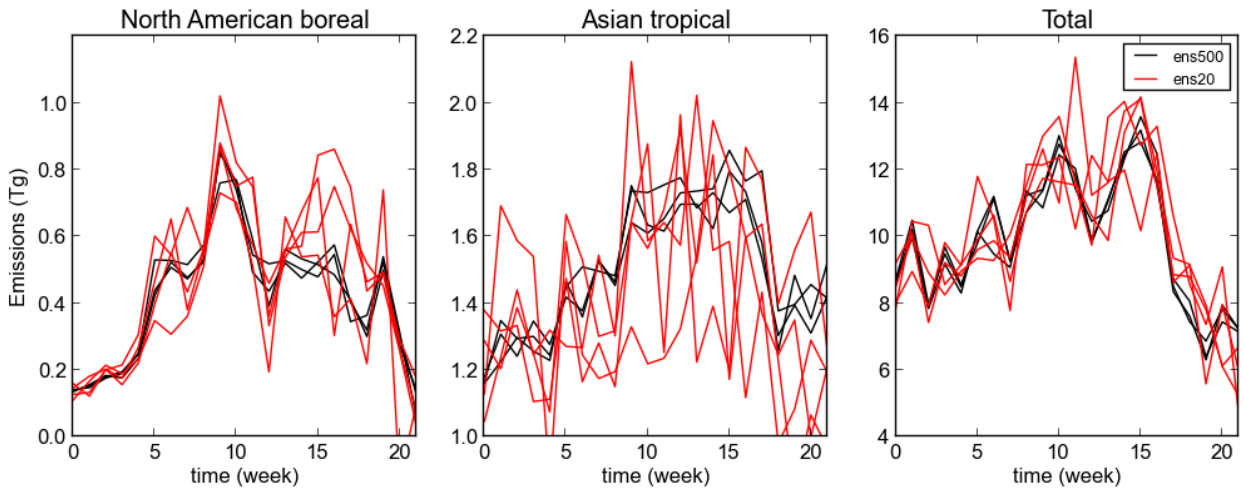

Figure 2: Weekly sum of the posterior mean biosphere and anthropogenic emissiond from six separate inversions with an ensemble size of 500 and 20 (three inversions for both sizes). For each line, the initial prior state vectors were sampled randomly from a normal distribution.

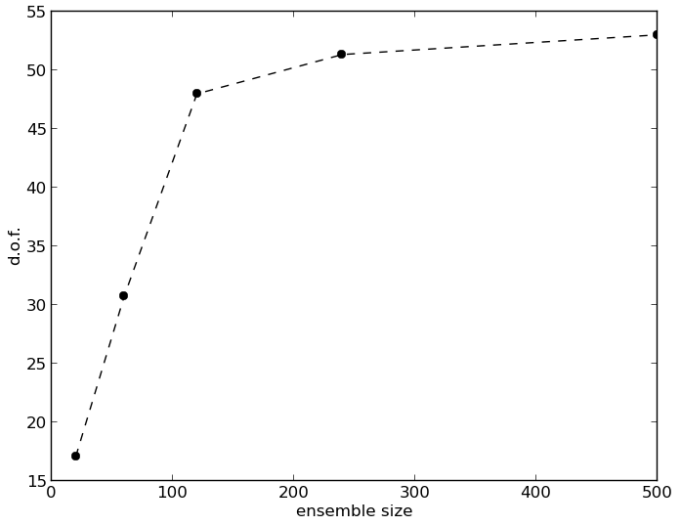

Figure 3: Number of degrees of freedom (d.o.f.) in the posterior ensemble as a function of number of ensemble size.

Geosci. Model Dev. Discuss., doi:10.5194/gmd-2016-181, 2016
Manuscript under review for journal Geosci. Model Dev.
Published: 19 August 2016
© Author(s) 2016. CC-BY 3.0 License.

Geoscientific Model Development Discussions
Open Access

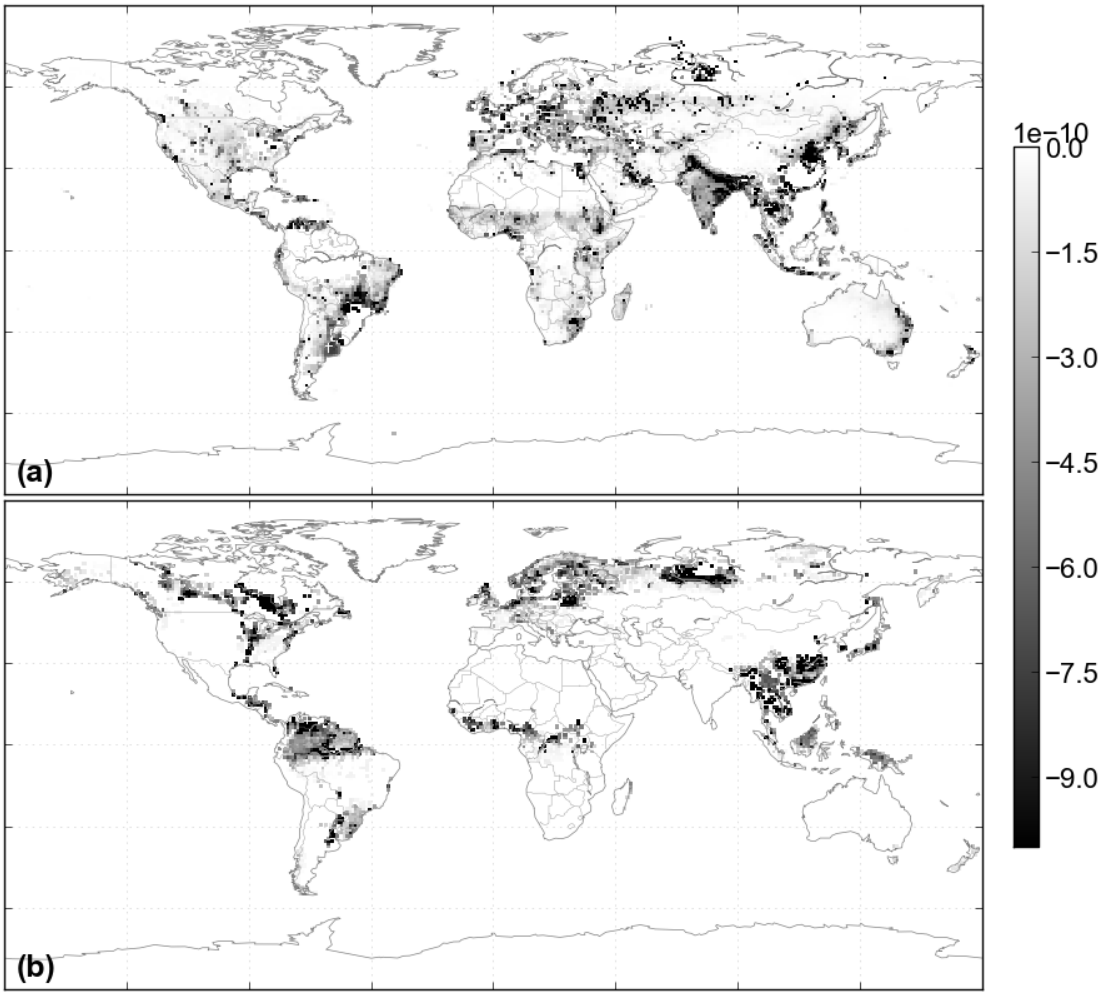

Figure 4: Differences in average uncertainty estimates between two runs, applying covariance matrices ***Q*1** and ***Q*2**, over the test period (mol/m^2/s), for (a) anthropogenic and (b) biosphere emissions. Negative values indicate smaller uncertainties using ***Q*2**.

Geosci. Model Dev. Discuss., doi:10.5194/gmd-2016-181, 2016
Manuscript under review for journal Geosci. Model Dev.
Published: 19 August 2016
© Author(s) 2016. CC-BY 3.0 License.

Geoscientific Model Development Discussions
Open Access

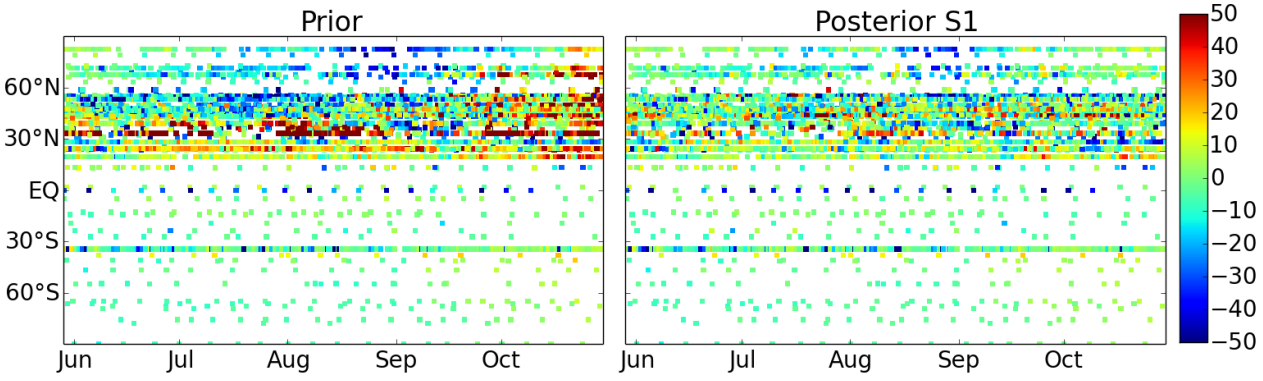

Figure 5: Differences between the modelled (prior, posterior S1) and observed atmospheric CH_4 mole fractions (observed – modelled) at the locations and sampling times of the assimilated observations from S1 (ppb). Positive values illustrate overestimation by the model.

Geosci. Model Dev. Discuss., doi:10.5194/gmd-2016-181, 2016
Manuscript under review for journal Geosci. Model Dev.
Published: 19 August 2016
© Author(s) 2016. CC-BY 3.0 License.

Geoscientific Model Development Discussions
Open Access

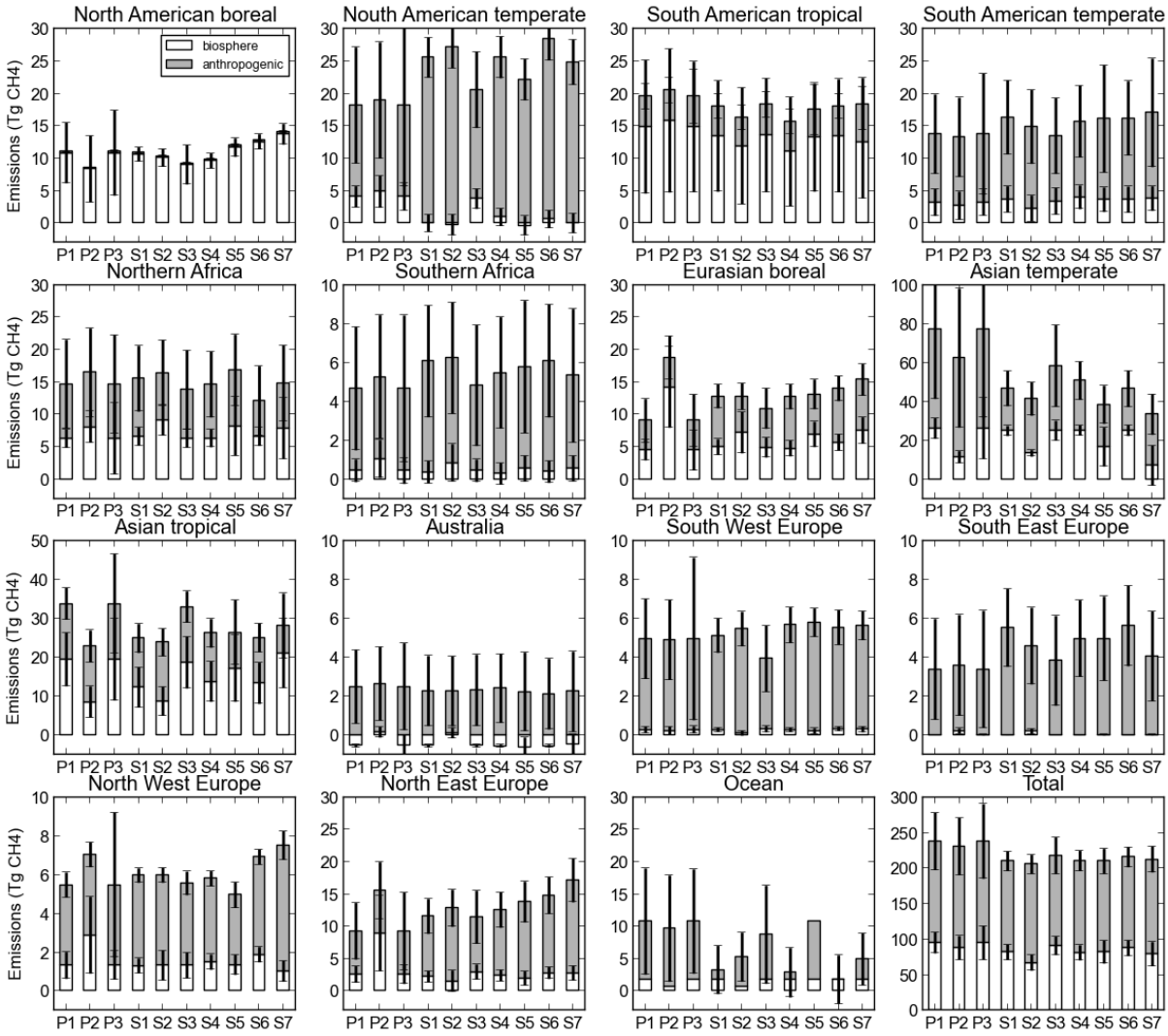

Figure 6: Estimated total emissions over the test period using several inversions. P1 – P3 are prior, and S1 – S6 are posteriors. P1 is used for S1, S3, S4 and S6, P2 is used for S2, and P3 for S5 and S7. Black bars illustrate the standard deviations of the ensemble members.

Geosci. Model Dev. Discuss., doi:10.5194/gmd-2016-181, 2016
Manuscript under review for journal Geosci. Model Dev.
Published: 19 August 2016
© Author(s) 2016. CC-BY 3.0 License.

Geoscientific Model Development Discussions
Open Access
EGU

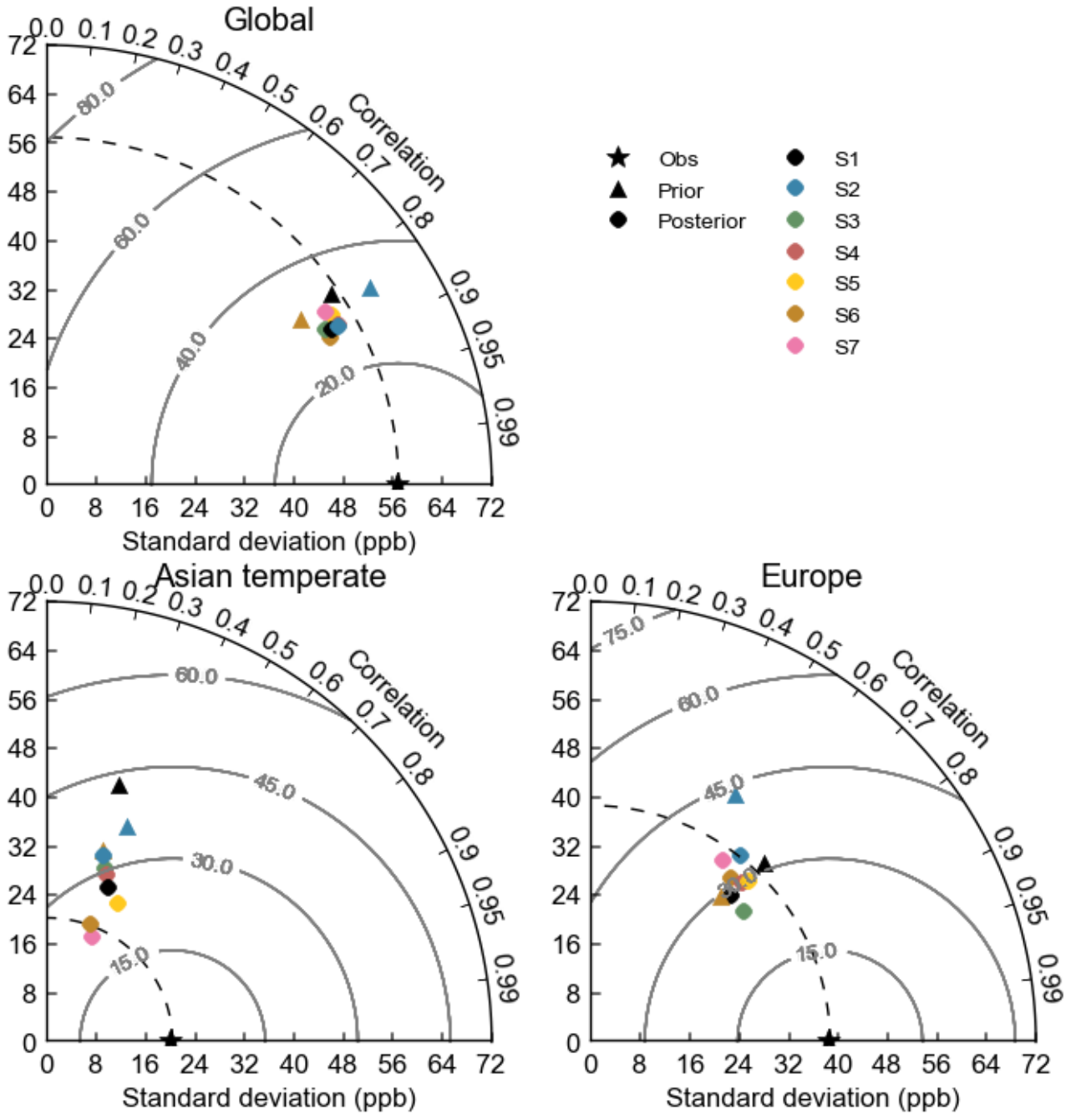

Figure 7: Taylor diagrams of atmospheric CH_4 mole fractions in different inversions. The NOAA discrete air sample observations are compared to the prior and posterior mole fractions. Note that the observations compared here were assimilated in all inversions.

Geosci. Model Dev. Discuss., doi:10.5194/gmd-2016-181, 2016
Manuscript under review for journal Geosci. Model Dev.
Published: 19 August 2016
© Author(s) 2016. CC-BY 3.0 License.

Geoscientific Model Development Discussions
Open Access

Table 1: List of surface in-situ observation sites used in inversions. Model-data-mismatch (mdm) is used in the observation covariance matrix, and defining rejection threshold of the observations. Data type is categorized into two: discrete (D), continuous (C) measurements.

Site Code	Station Name	Country/ Territory	Contributor	Latitude	Longitude	Elevation (m a.s.l.)	Mdm (ppb)	Data type (D/C)
ABP	Arembepe	Brazil	NOAA/ESRL	12.77°S	38.17°W	1.0	7.5	D
ALT	Alert	Canada	NOAA/ESRL	82.45°N	62.51°W	200.0	15.0	D
ALT	Alert	Canada	EC	82.45°N	62.51°W	200.0	15.0	C/D
AMS	Amsterdam Island	France	LSCE	37.95°S	77.53°E	150.0	7.5	D
AMT	Argyle	USA	NOAA/ESRL	45.03°N	68.68°W	50.0	30.0	D
AMY	Anmyeon-do	Korea	KMA	36.54°N	126.32°E	85.1	15.0	C
ARH	Arrival Heights	New Zealand	NIWA	77.80°S	166.67°E	184.0	7.5	D
ASC	Ascension Island	UK	NOAA/ESRL	7.97°N	14.42°E	85.0	7.5	D
ASK	Assekrem	Algeria	NOAA/ESRL	23.26°N	5.63°E	2710.0	25.0	D
AZR	Terceira Island	Portugal	NOAA/ESRL	38.77°N	27.37°W	19.0	15.0	D
BAL	Baltic Sea	Poland	NOAA/ESRL	55.35°N	17.22°E	3.0	75.0	D
BGU	Begur	Spain	LSCE	41.97°N	3.23°E	11.0	15.0	D
BHD	Baring Head	New Zealand	NOAA/ESRL	41.41°S	174.87°E	80.0	7.5	D
BKT	Bukit Koto Tabang	Indonesia	NOAA/ESRL	0.20°S	100.32°E	845.0	75.0	D
BME	St.David's Head	UK	NOAA/ESRL	32.37°N	64.65°W	12.0	15.0	D
BMW	Tudor Hill	UK	NOAA/ESRL	32.27°N	64.87°W	30.0	15.0	D
BRW	Barrow	USA	NOAA/ESRL	71.32°N	156.61°W	11.0	15.0	C/D
BSC	Black Sea	Romania	NOAA/ESRL	44.17°N	28.67°E	0.0	75.0	D
CBA	Cold Bay	USA	NOAA/ESRL	55.20°N	162.72°W	21.3	15.0	D
CDL	Candle Lake	Canada	EC	53.98°N	105.11°W	600.0	25.0	C
CFA	Cape Ferguson	Australia	CSIRO	19.28°S	147.05°E	2.0	25.0	D
CGO	Cape Grim	Australia	NOAA/ESRL	40.68°S	144.68°E	94.0	7.5	D
CHL	Churchill	Canada	EC	58.75°N	94.01°W	35.0	15.0	D
CHM	Chibougamau	Canada	EC	49.68°N	74.30°W	393.0	15.0	C
CHR	Christmas Island	Kiribati	NOAA/ESRL	1.70°N	157.15°W	0.0	7.5	D
COI	Cape Ochi-ishi	Japan	NIES	43.15°N	145.50°E	45.0	7.5	C
CPT	Cape Point	South Africa	SAWS	34.35°S	18.49°E	230.0	25.0	C
CRZ	Crozet	France	NOAA/ESRL	46.43°S	51.85°E	197.0	7.5	D
CYA	Casey Station	Australia	CSIRO	66.28°S	110.52°E	60.0	7.5	D
EGB	Egbert	Canada	EC	44.23°N	79.78°W	251.0	75.0	C
EIC	Easter Island	Chile	NOAA/ESRL	27.16°S	109.43°W	47.0	7.5	D
ESP	Estevan Point	Canada	EC	49.38°N	126.55°W	39.0	25.0	D
ETL	East Trout Lake	Canada	EC	54.35°N	104.98°W	492.0	25.0	C
FIK	Finokalia	Greece	LSCE	35.34°N	25.67°E	150.0	15.0	D
FSD	Fraserdale	Canada	EC	49.88°N	81.57°E	210.0	15.0	C

Geosci. Model Dev. Discuss., doi:10.5194/gmd-2016-181, 2016
Manuscript under review for journal Geosci. Model Dev.
Published: 19 August 2016
© Author(s) 2016. CC-BY 3.0 License.

GMI	Guam	USA	NOAA/ESRL	13.38°N	144.65°E	0.0	15.0	D
GSN	Gosan	Korea	NIER	33.28°N	126.15°E	72.0	15.0	C
HAT	Hateruma	Japan	NIES	24.05°N	123.80°E	10.0	15.0	C
HBA	Halley Bay	UK	NOAA/ESRL	75.60°S	26.21°W	30.0	7.5	D
HPB	Hohenpeissenberg	Germany	NOAA/ESRL	47.80°N	11.02°E	936.0	25.0	D
HUN	Hegyhatsal	Hungary	NOAA/ESRL	46.95°N	16.65°E	248.0	75.0	D
ICE	Heimaey	Iceland	NOAA/ESRL	63.40°N	20.29°W	118.0	15.0	D
IZO	Izaña	Spain	NOAA/ESRL	28.31°N	16.50°W	2372.9	15.0	D
IZO	Izaña	Spain	AEMET	28.31°N	16.50°W	2372.9	15.0	C
JFJ	Jungfraujoch	Switzerland	EMPA	46.55°N	7.98°E	3570.0	15.0	C
KEY	Key Biscayne	USA	NOAA/ESRL	25.67°N	80.15°W	1.0	25.0	D
KMW	Kollumerwaard	Netherlands	RIVM	53.33°N	6.26°E	0.0	15.0	C
KUM	Cape Kumukahi	USA	NOAA/ESRL	19.52°N	154.82°W	3.0	7.5	D
KZD	Sary Taukum	Kazakhstan	NOAA/ESRL	44.08°N	76.87°E	595.0	75.0	D
KZM	Plateau Assy	Kazakhstan	NOAA/ESRL	43.25°N	77.88°E	2519.0	25.0	D
LAU	Lauder	New Zealand	NIWA	45.04°N	169.68°E	370.0	15.0	C
LLB	Lac La Biche	Canada	EC	54.95°N	112.45°W	540.0	75.0	C
LLN	Lulin	China	NOAA/ESRL	23.47°N	120.87°E	2862.0	25.0	D
LMP	Lampedusa	Italy	NOAA/ESRL	35.52°N	12.62°E	45.0	25.0	D
LPO	Ile Grande	France	LSCE	48.80°N	3.58°W	10.0	15.0	D
MAA	Mawson	Australia	CSIRO	67.62°S	62.87°E	32.0	7.5	D
MHD	Mace Head	Ireland	NOAA/ESRL	53.33°N	9.90°W	5.0	25.0	D
MID	Sand Island	USA	NOAA/ESRL	28.21°N	177.38°W	11.0	15.0	D
MLO	Mauna Loa	USA	NOAA/ESRL	19.54°N	155.58°W	3397.0	15.0	C/D
MNM	Minamitorishima	Japan	JMA	24.28°N	153.98°E	8.0	15.0	C
MQA	Macquarie Island	Australia	CSIRO	54.48°S	158.97°E	12.0	7.5	D
NGL	Neuglobsow	Germany	UBA	53.14°N	13.03°E	62.0	15.0	C
NMB	Gobabeb	Namibia	NOAA/ESRL	23.58°S	15.03°E	456.0	25.0	D
NWR	Niwot Ridge	USA	NOAA/ESRL	40.05°N	105.59°W	3523.0	15.0	D
OXK	Ochsenkopf	Germany	NOAA/ESRL	50.03°N	11.80°E	1009.0	15.0	D
PAL	Pallas-Sammaltunturi	Finland	NOAA/ESRL	67.58°N	24.06°E	565.0	15.0	D
PAL	Pallas-Sammaltunturi	Finland	FMI	67.58°N	24.06°E	565.0	15.0	C
PDM	Picdu Midi	France	LSCE	42.94°N	0.14°E	2877.0	15.0	D
PSA	Palmer Station	USA	NOAA/ESRL	64.92°S	64.00°W	10.0	7.5	D
PTA	Point Arena	USA	NOAA/ESRL	38.95°N	123.74°W	17.0	25.0	D
PUY	Puyde Dome	France	LSCE	45.7°N	2.97°E	1465.0	15.0	D
RPB	Ragged Point	Barbados	AGAGE	13.17°N	59.43°W	15.0	15.0	D
RYO	Ryori	Japan	JMA	39.03°N	141.82°E	260.0	15.0	C
SEY	Mahe Island	Seychelles	NOAA/ESRL	4.68°S	55.53°E	2.0	7.5	D
SGP	Southern Great Plains	USA	NOAA/ESRL	36.60°N	97.49°W	314.0	75.0	D

Geosci. Model Dev. Discuss., doi:10.5194/gmd-2016-181, 2016
Manuscript under review for journal Geosci. Model Dev.
Published: 19 August 2016
© Author(s) 2016. CC-BY 3.0 License.

SHM	Shemya Island	USA	NOAA/ESRL	52.71°N	174.13°E	23.0	25.0	D
SMO	Tutuila	USA	NOAA/ESRL	14.25°S	170.56°W	42.0	7.5	D
SPO	South Pole	USA	NOAA/ESRL	89.98°S	24.80°W	2810.0	7.5	D
SSL	Schauinsland	Germany	UBA	47.90°N	7.91°E	1205.0	15.0	C
STM	Ocean Station M	Norway	NOAA/ESRL	66.00°N	2.00°E	0.0	15.0	D
SUM	Summit	Denmark	NOAA/ESRL	72.60°N	38.42°W	3209.5	15.0	D
SYO	Syowa Station	Japan	NOAA/ESRL	69.01°S	39.59°E	14.0	7.5	D
TAP	Tae-ahn Peninsula	Korea	NOAA/ESRL	36.74°N	126.13°E	16.0	75.0	D
TDF	Tierradel Fuego	Argentina	NOAA/ESRL	54.85°S	68.31°W	12.0	7.5	D
TER	Teriberka	Russia	MGO	69.20°N	35.10°E	40.0	15.0	D
THD	Trinidad Head	USA	NOAA/ESRL	41.05°N	124.15°W	107.0	7.5	D
UTA	Wendover	USA	NOAA/ESRL	39.90°N	113.72°W	1327.0	25.0	D
UUM	Ulaan Uul	Mongolia	NOAA/ESRL	44.45°N	111.10°E	1007.0	25.0	D
WIS	Sede Boker	Israel	NOAA/ESRL	30.85°N	34.78°E	477.0	25.0	D
WKT	Moody	USA	NOAA/ESRL	31.31°N	97.33°W	251.0	30.0	D
WLG	Mt. Waliguan	China	NOAA/ESRL	36.28°N	100.90°E	3810.0	15.0	D
WSA	Sable Island	Canada	EC	43.93°N	-60.02°W	5.0	25.0	C/D
YON	Yonagunijima	Japan	JMA	24.47°N	123.02°E	30.0	15.0	C
ZEP	Zeppelinfjellet	Norway	NOAA/ESRL	78.91°N	11.89°E	474.0	15.0	D
ZSF	Zugspitze/ Schneefernerhaus	Germany	UBA	47.41°N	10.97°E	2671.0	15.0	C

Table 2: Reference (S1) and sensitivity inversion set-ups.

Inversion	Number of state vectors (model)	Observations	Prior bio	TM5	Assimilation window length
S1	M1	discrete+continuous	LPX-Bern	Tiedtke (1989)	5 weeks
S2	M1	discrete+continuous	LPJ-WHyME	Tiedtke (1989)	5 weeks
S3	M1	discrete	LPX-Bern	Tiedtke (1989)	5 weeks
S4	M1	discrete+continuous	LPX-Bern	Tiedtke (1989)	12 weeks
S5	M2	discrete+continuous	LPX-Bern	Tiedtke (1989)	5 weeks
S6	M1	discrete+continuous	LPX-Bern	Gregory *et al.* (2000)	5 weeks
S7	M2	discrete+continuous	LPX-Bern	Gregory *et al.* (2000)	5 weeks

Table 3: Prior emission estimates and their uncertainties (Tg CH_4/test period). Note that the fire, termites and ocean emissions are not optimized, i.e. no uncertainties associated with their estimates. P1 is used as prior for S1, S3, S4, and S6. P2 is used as prior for S2. P3 is used as prior for S5 and S7. *[1] the difference between air and seawater partial pressure of methane

Emission	Reference	P1	P2	P3
Anthropogenic	EDGAR v4.2 FT2010	142 ± 40	142 ± 40	142 ± 52
Biosphere	LPX-Bern (P1,P3), LPJ-WHyME (P2)	95 ± 15	88 ± 17	95 ± 24

Geosci. Model Dev. Discuss., doi:10.5194/gmd-2016-181, 2016
Manuscript under review for journal Geosci. Model Dev.
Published: 19 August 2016
© Author(s) 2016. CC-BY 3.0 License.

Fire	GFED v3.2	11 ± –	11 ± –	11 ± –
Termites	Ito *et al.* (2012)	9 ± –	9 ± –	9 ± –
Ocean	Lambert and Schmidt (1993)*[1], ECMWF ERA-Interim	26 ± –	26 ± –	26 ± –
Total		284 ± 43	153 ± 44	284 ± 58

Table 4: Estimated global posterior emissions and their uncertainties from inversions S1-S7 (Tg CH_4/test period). Note that the total emissions are the sum of the anthropogenic and the biosphere emissions.

Emission\Inversion	S1	S2	S3	S4	S5	S6	S7
Anthropogenic	128 ± 14	138 ± 13	127 ± 26	129 ± 14	128 ± 18	128 ± 14	133 ± 18
Biosphere	82 ± 11	67 ± 11	91 ± 13	81 ± 11	82 ± 16	88 ± 11	80 ± 17
Total	210 ± 16	206 ± 16	218 ± 28	211 ± 16	210 ± 19	216 ± 17	213 ± 21